Article

Solar Hydrogen Variable Speed Control of Induction Motor Based on Chaotic Billiards Optimization Technique

Basem E. Elnaghi [1,*], M. N. Abelwhab [1], Ahmed M. Ismaiel [1] and Reham H. Mohammed [2]

[1] Electrical Power and Machines Department, Faculty of Engineering, Suez Canal University, Ismailia 41522, Egypt

[2] Electrical Engineering Department, Faculty of Engineering, Suez Canal University, Ismailia 41522, Egypt

* Correspondence: basem_elhady@eng.suez.edu.eg

Abstract: This paper introduces a brand-new, inspired optimization algorithm (the chaotic billiards optimization (C-BO) approach) to effectively develop the optimal parameters for fuzzy PID techniques to enhance the dynamic response of the solar–hydrogen drive of an induction motor. This study compares fuzzy-PID-based C-BO regulators to fuzzy PID regulators based on particle swarm optimization (PSO) and PI-based PSO regulators to provide speed control in solar–hydrogen, induction-motor drive systems. The model is implemented to simulate the production and storage of hydrogen while powering an induction-motor drive which provides a great solution for the renewable energy storage problem in the case of solar pumping systems. MATLAB/Simulink 2021a is used to simulate and analyze the entire operation. The laboratory prototype is implemented in real time using a DSP-DS1104 board. Based on the simulation and experimental results, the proposed fuzzy-PID-based C-BO has reduced speed peak overshoot by 45.3% when compared to a fuzzy PID based PSO speed regulator and by 68.13% when compared to a PI-based PSO speed controller in the case of a large-scale motor. Additionally, the proposed speed regulator has a 6.1% faster speed rising time than a fuzzy-PID-based PSO and a 9.5% faster speed rising time than a PI–PSO speed controller. It has an excellent dynamic responsiveness value when compared to the other speed regulators.

Keywords: hydrogen production; chaotic billiards optimization; particle swarm optimization; solar–hydrogen induction motor drive; electrolysis; field-oriented control

1. Introduction

World transport relies heavily on oil, which supplies 95% of the overall electricity and accounts for approximately one-fourth of global emissions. Naval ships that use fossil fuels continue to pollute the environment all around the planet. During the previous decade, transportation pollution grew at a greater rate than other power sectors. Global transportation activity will continue to rise in tandem with economic expansion. Ocean transport has long dominated global freight, with ships growing in size and quantity. Fossil-fuel consumption also poses many critical issues and problems, such as climate change and increased supply costs; for example, in 2002, the use of fossil fuels accounted for 85% of the worldwide energy use. In 2003, electrical energy needs in the U.S.A. reached a high value of 24% [1,2]. Fossil-fuel use is the primary source of CO_2. CO_2 can also be emitted from direct, human-induced impacts on forestry and other land use, such as deforestation, land clearing for agriculture, and the degradation of soils. Likewise, land can also remove CO_2 from the atmosphere through reforestation, the improvement of soils, and other activities. The need for energy has increased exponentially as a result of the rapid growth of the world's population and advancements in civilization. Despite being unsustainable and having serious issues with respect to the environment and human health [3,4], fossil fuels continue to dominate the global energy market. When fossil fuels

are burned, many greenhouse gases, including methane, carbon dioxide, and nitrous oxide, are released into the atmosphere. As a result of the quick pace of civil and industrial growth, it is also anticipated that the emissions of these gases will rise with time. If energy sources remain the same, the current and predicted levels of greenhouse gases will cause weather changes, serious health issues, a rise in sea levels, and changes in the environment, etc. [5]. Humans are in danger from the climate change and health issues brought on by fossil-fuel use [6,7]. In light of these facts, all countries have begun to develop a number of efforts to prevent these catastrophes. To lessen these issues, governments have begun revising their energy strategies and regulations. Hydrogen has begun to play an important role as a future energy carrier. The importance of hydrogen in the future infrastructure of energy generation is demonstrated through clean energy generation using technologies such as fuel cells. This could be a major impediment to the growth of such technologies. The separation of H_2O molecules into H_2 and O_2 is known as water electrolysis. This technology has great potential and holds great promise for sustainable fuel production [8]. The contents of this article are as follows: the three forms of water electrolysis are explained. The purpose of this article is to enhance the effects of electrolysis-mechanism modeling and to obtain simulated results. The hydrogen was generated and stored in the tank. The mathematical model of the electrolysis was developed using the MATLAB/Simulink package. The effect of using a DC/DC, current-controlled buck converter was estimated. The FOC method for induction machines is one of the most commonly used control methods for induction machines that require a high-dynamic performance. Optimization techniques have been used in several studies to improve the performance of control systems; for instance, FLC design-optimization techniques use a differential search algorithm optimization to develop an FLC [9–11]. In order to increase the efficiency of the pumping system, Saady and Ikram, et al. introduced a freestanding, photovoltaic (PV) water-pumping system (PVWPS) powered by an induction motor without energy storage. The perturb and observe (P&O) method and the incremental conductance (INC) MPPT method with a variable, automatically adjusted step size are compared first [12]. Error, Mustapha, and Aziz Derouich investigated a centrifugal pump and a three-phase, asynchronous-motor solar-pumping system. The water flow was managed using a field-oriented control [13]. This continues to be an intriguing and challenging topic for further research. The simplicity of the FOC is emphasized; the only induction-machine parameter required is the stator resistance. The control variables—namely, the electromagnetic torque and the flux vector of the stator—are directly regulated, and current regulators or SVM signal generators are needed [14,15]. In order to enhance the performance of a three-phase, induction-motor drive system powered by a standalone PV power source, Sobhy S. Dessouky and his colleagues suggested a modified control technique in [16]. The three primary goals of the suggested control technique were to (1) ensure successful motor starting; (2) match the on-site induction-motor pumping load with the available PV power, and (3) force the PV system to run at its peak power. The perturb and observe (P&O) technique served as the foundation for the maximum power point tracking (MPPT). PV power panels, a three-phase inverter, a three-phase induction motor, a DC/DC boost converter, and a DC link capacitor made up the system. In [17], Bhim Singh and colleagues described a straightforward and effective induction motor drive (IMD)-based, solar photovoltaic (PV) water-pumping system. Two phases of power conversion were used in this solar-powered, PV water-pumping system. The first stage regulated the duty ratio of a DC/DC boost converter to obtain the most power possible out of a solar PV array. The motor speed was managed to maintain the dc bus voltage. By lowering the motor currents at the greater voltage for the same power injection, this control aided in the reduction of motor losses. An incremental, conductance-based maximum power point tracking (MPPT) control approach was used to regulate the duty ratio. The PV-supplied, three-phase induction motor (IM) water-pumping system provides a single-stage solution, according to Ramulu Chinthamalla et al. in [18]. The suggested approach employed two tried-and-true two-level, cascaded H-bridge inverters to provide the IM pump drive

with a three-level voltage output. The suggested system was run utilizing a control method that combined V/f control, space vector pulse width modulation (SVPWM), and maximum power point tracking (MPPT). Under an order to run the cascaded inverter and provide a three-level output voltage for all environmental situations, the MPPT algorithm produced the modulation index "ma." The design and implementation of a solar-powered, single-phase, capacitor-start induction motor were presented by Syed Rahman and his colleagues in [19]. A single-phase induction motor's power supply from a photovoltaic (PV) array was managed by a multilevel quasi-impedance source inverter. The primary challenge with solar-powered drive systems is the steady, intended operation of the drive when confronted with changes in the PV-array power output. To ensure the efficient integration of renewable technologies into the power grid and to pave the way for their progressive incorporation into future energy scenarios, one of the major obstacles to be addressed is the storage of electricity from renewable energy sources. The use of hydrogen as an energy carrier is a practical and promising choice among the several technologies that may be utilized to store electrical energy from renewable sources on a large scale. The majority of hydrogen storage facilities for renewable energy now use electrolysis systems that are connected to the power source, which is frequently solar or wind energy. In order to use hydrogen in stationary fuel cells to generate electricity, hydrogen is stored in line with the facility requirements [20]. The size optimization of a grid-connected, hybrid photovoltaic/fuel-cell power system with hydrogen storage is discussed by M.S. Okundamiya in [21]. The main goal is to size a hybrid power system as efficiently as possible to meet the load demand of a university lab with an unpredictable grid at the lowest possible cost of energy and with the lowest amount of carbon emissions. A clean and sustainable energy system will replace the grid-connected diesel power system. By utilizing HOMER's energy-balance methodologies, an ideal design architecture was created (a hybrid optimization model for electric renewables).

Zeb et al. compared the performance of their smart control system for induction motors (IM) to that of a traditional PI speed controller. Their system used an adaptive fuzzy logic controller (AFLC) based on the Levenberg–Marquardt algorithm [22], which has an integral square error of 2.986. In numerous technical applications, a variety of optimization techniques were developed for fine-tuning fuzzy-logic controllers, including the genetic algorithm [23]; grey-wolf optimizer [24]; whale-optimization algorithm [25]; and intelligence-based fuzzy methods such as the fuzzy logic controller [26]; fuzzy–genetic controller [27]; swarm-optimization- and pattern-search-based fuzzy controller [28]; and a differential-evolution-based fuzzy controller [29], which were applied to tune the PI controllers' gain used in several power applications. Moreover, metaheuristic techniques such as the cuckoo search algorithm [30], particle swarm optimization (PSO) [31], PSO-sine-cosine-based swarm optimization (PSO-SCSO) [32], and the bees algorithm [33] are viable options for fine-tuning the settings of fuzzy logic controllers. All these research studies have provided fresh approaches to speed-controller optimization, although they do so with comparatively large integral-square errors and poor convergence rates. Table 1 shows the main advantages and disadvantages of the old optimization methods.

Table 1. Old optimization techniques.

Optimization Technique	Advantages	Disadvantages
Levenberg–Marquardt algorithm [22]	- Fitness function will decrease after every iteration. - Decreases cost most quickly for a given change in parameter values.	- The algorithm tends to zig-zag along the bottom of long, narrow canyons. - Approaches the best fit very slowly.
Genetic algorithm [23]	The concept is easy to understand.	It requires less information about the problem, but designing an objective function

	GA search is performed from a population of points, not a single point. GA uses payoff (objective function) information, not derivatives.	and obtaining the correct representation and operators can be difficult. It is computationally expensive, i.e., time-consuming.
Grey-wolf optimizer [24]	Fewer parameters, simple principles, and is implemented easily.	Low convergence speed, low solution accuracy, and easily falls into the local optimum.
Whale-optimization algorithm [25]	Stronger global search ability and better stability.	Low convergence and easy localization.
Cuckoo search algorithm [30]	Easier to apply, has fewer tuning parameters.	It has proven to very easily fall into local optimal solutions and has a slow rate of convergence.
Particle swarm optimization [31]	Has rapid convergence and fewer tuning parameters.	They often converge to some local optimization.

The revolutionary, novel physics metaheuristic optimization method known as the "billiards optimizer algorithm" (BOA) was inspired by the widely played game of pool. It was first presented in 2020 [34] by Kaveh et al. In the billiards optimization algorithm, the pockets are represented by the optimum solutions obtained and each solution is represented by a billiards ball. Using vector algebra and conservation rules, the final positions of the balls in the optimization process are established if any ball strikes other balls. The BOA was effectively used to solve twenty-three mathematical functions and seven limited engineering benchmark tasks [34]. In the C-BO approach, chaotic logistic maps (CLMs) are integrated with the BOA to improve the overall performance of the algorithm. The initialization process is unable to produce a useful beginning method for the optimization process due to the initial circumstances and population (agents) selection at random of the meta-heuristic approach. Consequently, selecting the ideal starting conditions may improve their overall characteristics. As a result, the agents are rearranged using chaotic logistic maps to improve the initialization procedure. As a result, the authors provide the BOA with a chaotic character to reinforce it. The C-BO algorithm stands out from other algorithms thanks to its low design-parameter requirements, straightforward construction, light computing load, quick convergence speed, and capacity to address a wide range of optimization issues in various engineering applications.

In order to correctly design the fuzzy PID speed regulators for the stability improvement of speed performance, this article provides a novel C-BO method. The induction motor is connected to various mechanical loadings. The control methodology for these VSCs is a fuzzy PID approach that has been suitably adjusted by the C-BO. At a quick convergence speed, the C-BO algorithm adjusts the gains of several fuzzy PIDs used in the system. The integrated square error is used as the objective function in a simulation-based optimization strategy. The augmentation of transient parameters, such as the settling time (Ts), maximum over/undershoots (Mp), and the steady-state error (Ess) of the speed, is a part of the stability improvement of the system. By conducting the analysis both experimentally and theoretically, the validity of the proposed control strategy is thoroughly examined.

To the best knowledge of the authors, neither the literature on power systems nor the literature on renewable energy sources have mentioned the solar–hydrogen drive for induction motors or the fuzzy-PID-based C-BO for induction motor drives.

In this paper, the main contributions are summarized as follows:

(1) Present the optimum design of a fuzzy-PID-based C-BO, which is used as speed regulator in a solar–hydrogen drive for induction-motor speed control;
(2) Validate the novel application of a solar–hydrogen drive for induction motor speed and torque regulation;
(3) Model the solar–hydrogen speed drive for an induction motor using Matlab/Simulink 2021a;
(4) Examine the electrolysis features of PEM in various air conditions as a part of the proposed model;
(5) Minimize the multi-dimensional objective-fitness function and the optimized objectives to achieve the minimum for speed-tracing torque-tracking errors, peak overshoot, rising time, and steady-state errors for speed and torque responses;
(6) The proposed fuzzy-PID-based C-BO has reduced the speed-peak overshoot by 45.3% when compared to a fuzzy PID—PSO speed regulator and by 68.13% when compared to a PI–PSO speed controller in the case of a large-scale motor;
(7) The proposed speed regulator has a 6.1% faster speed-rising time than a fuzzy-PID-based PSO and a 9.5% faster speed rising time than a PI–PSO speed controller;
(8) Investigate the system using Matlab/Simulink 2021a and investigate it experimentally using DSpace 1104 to demonstrate the robustness and enhancement of C-BO-based fuzzy PID against fuzzy PID based PSO.

The remainder of this paper is organized as follows. In Section Two, we first discuss the hydrogen production methods based on a renewable energy source and provide a complete comparison between water electrolysis technologies. In Section Three, we first describe the system model and formulate the optimization problem. The proposed C-BO algorithm is described in Section Four. A tuning- and simulation-process-based C-BO algorithm is discussed in Section Five. After demonstrating the performance of the Simulink setup in Section Six, we discuss the simulation results for two different motors in Section Seven using Matlab/Simulink 2021a. After validating the proposed model in a laboratory experiment using DSpace1104 in Section Eight, we conclude this paper in Section Nine.

2. Hydrogen Production

Hydrogen is regarded as a good way to store the electrical energy produced by alternative energy sources. When compared to alternative electric-energy storage technologies such as batteries, hydrogen demonstrates durability and a massive, intrinsic mass–energy density. This shows that combining hydrogen systems with renewable energy systems is a viable solution to the intermittent nature of renewable energy. As the potential of localized renewable-energy sources exceeds the gigawatt scale, a storage device of comparable capacity is required [35,36].
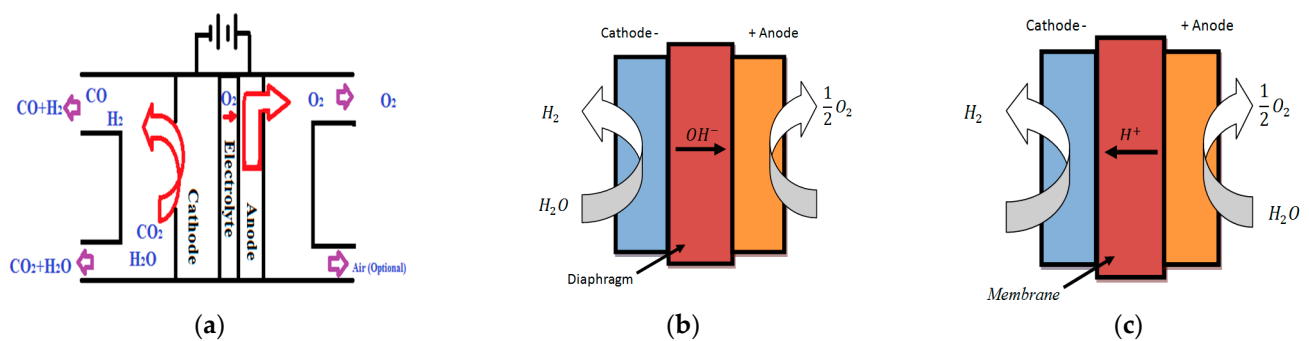
Water Electrolysis

This section is designed to summarize the main differences between electrical water electrolysis technologies and determine which one is most suitable for this research. There four main types of water electrolysis: solid oxide electrolysis, alkaline electrolysis, proton exchange membrane electrolysis, and high temperature electrolysis.

SOECs are essentially a solid oxide fuel cells (SOFCs) that work in reverse, as is shown in Figure 1a. They can be used to create hydrogen from the surplus energy produced by, for example, wind turbines. SOECs may also electrolyze CO_2 to produce carbon monoxide (CO). When water and electricity are electrolyzed simultaneously, a combination of hydrogen and CO is produced. This combination, called syngas, is the starting point for a range of hydrocarbon syntheses [36,37].

Although alkaline electrolysis is one of the easiest methods for making hydrogen, it is also a very expensive process. Furthermore, electrolysis is a green, energy-producing technique that will become increasingly important in the future. A "diaphragm" separates

the two electrodes shown in Figure 1b. To maintain safety, this component works to separate the product gases from one another. The hydroxide ions and water molecules are also passed by this diaphragm [37].

In 1960s, General Electric developed the first PEM electrolysis system using a solid-polymer electrolyte. The primary purpose of this type of electrolysis was to eliminate the drawbacks of alkaline electrolysis [35]. The PEM also has a compact system design, as is shown in Figure 1c [37].


Figure 1. (**a**) Solid oxide electrolysis (SOEC), (**b**) alkaline water electrolysis, and (**c**) PEM water electrolysis.

Westinghouse [38,39] in North America and Lurgi and Dornier in Germany developed the high-temperature electrolysis of water vapor as part of the HOT ELLY (High Operating Temperature ELectroLYsis) project at approximately the same time (1975–1987). Due to the fact that almost all solid oxide cells (SOCs) are reversible at these high temperatures and can be used as either SOECs or SOFCs, relying on the operation mode, an interest in high-temperature electrolysis has exploded in the wake of significant progress in the SOFC field. However, in Germany and elsewhere, projects are still in the early stages of development [40,41].

Therefore, PEM electrolysis is a perfect choice for the proposed model because it has high current densities, a high voltage efficiency, a simple system configuration, a grid stability that requires a lightning-fast system response, and high-pressure operation that is possible thanks to its compact stack design [42].

3. Proposed Model Setup

As is illustrated in Figure 2, the electrical power for the induction motor drive is provided by a PEM fuel cell which converts the hydrogen into electrical power plus water, which is sent to a water tank. The hydrogen gas is produced by PEM electrolysis, which converts water into hydrogen for later use. PEM electrolysis is powered by a DC/DC-current source converter which produces a constant current from a PV solar-cell array. PEM electrolysis is being analyzed under different currents and various atmospheric conditions. The PEM fuel cell powers the voltage source inverter (VSI), which is controlled using a variable-frequency controller that is based on a field-oriented controller. The proposed system allows for the continuous operation of solar induction motor drives under no radiation. The frequency controller is implemented using fuzzy PID-based C-BO. The fuzzy PID-based C-BO is compared to fuzzy-PID-based PSO and PI–PSO speed regulators.
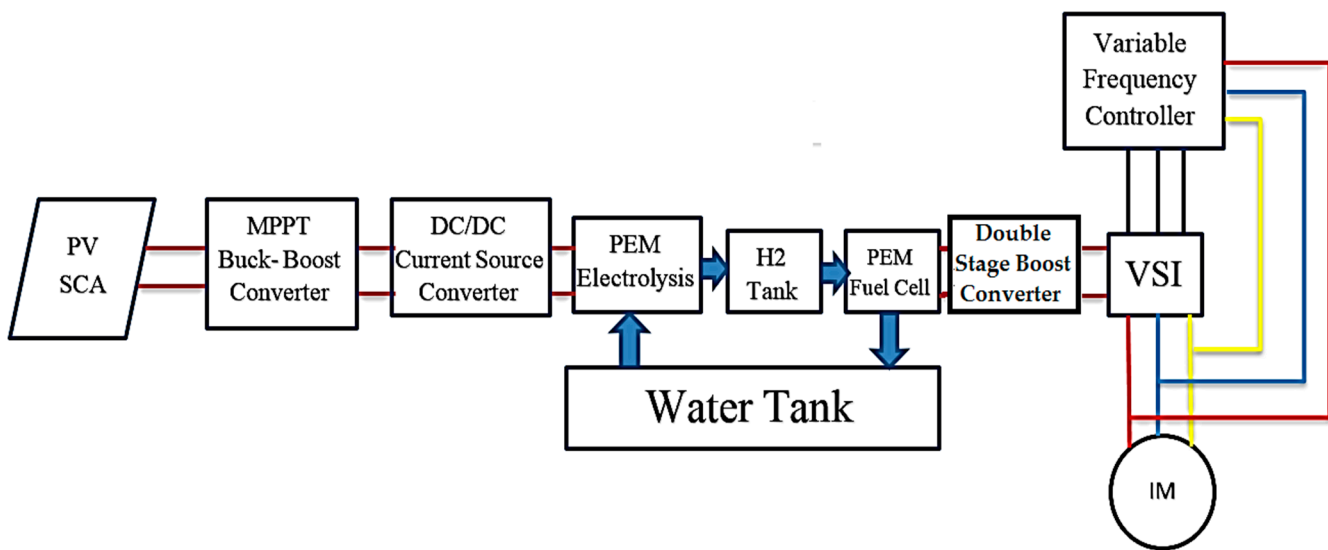
Figure 2. Proposed setup.

3.1. Photovoltaic Panel

Photovoltaic solar energy is generated by turning sunlight into electricity using a photoelectric-effect-based technology. It is a type of renewable, limitless, and non-polluting energy that may be generated in a variety of facilities ranging from modest self-consumption generators to large solar plants. It is important to learn how these massive solar fields function. Any solar cell's physical behavior is extremely similar to that of a typical p-n junction diode [43]. The solar cell's electrical equivalent circuit is seen in Figure 3.
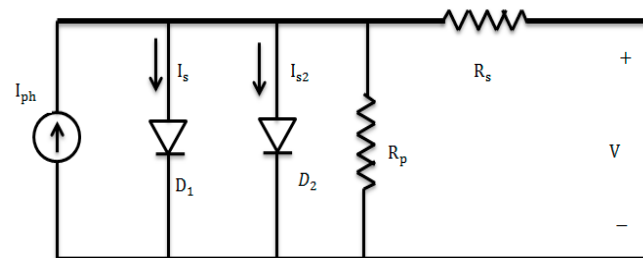

Figure 3. The solar cell electrical equivalent circuit.

The following formula may be used to find the relationship between the output current, I, and the output voltage, V [43]:

$$I = I_{ph} - I_s \left(e^{\frac{V+IR_s}{N_1 V_t}} - 1 \right) - I_{s2} \left(e^{\frac{V+IR_s}{N_1 V_t}} - 1 \right) - \frac{V + IR_s}{R_p} \tag{1}$$

the I–V and P–V characteristic curves of the PV panel were employed in this study with irradiances of 1 kW/m², 0.6 kW/m², and 0.1 kW/m² at 25 °C and 50 °C, as is shown in Figure 4. The proposed solar-array parameters are given in Table 2. Temperature is important in solar energy as the four factors (I_r, R_s, I_s, and V_t) are all functions of temperature It is apparent that the lower the temperature becomes, the more solar energy is generated [44].
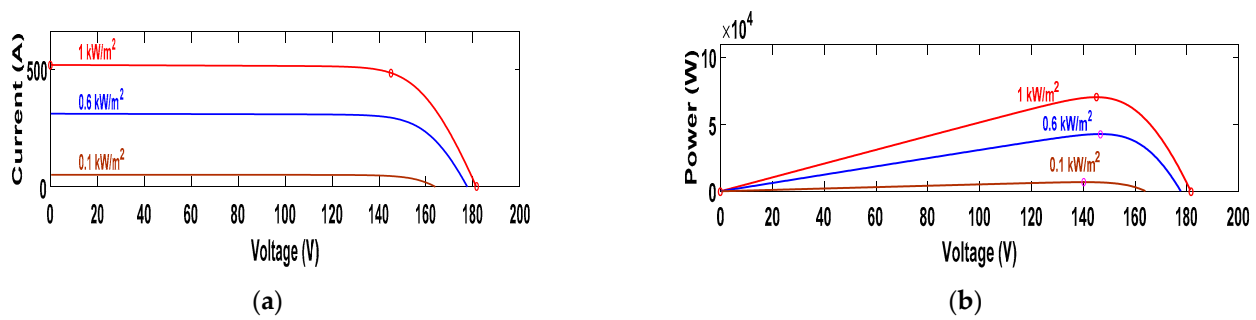
Figure 4. PV solar array at 1 kW/m², 0.6 kW/m², and 01 kW/m² for the (**a**) I–V curve and (**b**) P–V curve.

Table 2. Specifications of the PV system.

Parameters	Value
No. of series PV modules	5
No. of parallel PV strings	66
Module Maximum Power	213.15 w
Module open-circuit voltage (V_{oc})	36.3 V
Module short-circuit current (I_{sc})	7.84 A
Module maximum power point voltage (V_{mpp})	29 V
Module maximum power point current (I_{mpp})	7.35 A
Temperature	25 C
Irradiance	1000 W/m²

3.2. Maximum Power Point Tracking

One of the most effective methods for tracking the module MPP is the incremental conductance (IC) technique. This technique attempts to improve the tracking time and produce more energy in an environment that is changing due to irradiation by determining the maximum power point by utilizing the rate of change of power with regard to the voltage (dP/dV). The relationship between dI/dV and $-I/V$, in addition to the above derivative, is an important aspect in the IC methodology. The output control signal of the IC method is used to adjust the voltage reference of the PV array by increasing or decreasing a constant value ($\Delta V = \delta$) to the previous reference voltage. The basic equations of this method are as follows

$$\frac{dI}{dV} = -\frac{I}{V} \quad Module\ power\ is\ at\ MPP \tag{2}$$

$$\frac{dI}{dV} < -\frac{I}{V} \quad Module\ power\ is\ Right\ of\ MPP \tag{3}$$

$$\frac{dI}{dV} > -\frac{I}{V} \quad Module\ power\ is\ left\ of\ MPP \tag{4}$$

3.3. Current Controlled Converter

This converter is referred to as a DC/DC step-down buck converter. The output voltage is reduced when compared to the input voltage. As is illustrated in Figure 5, a buck converter was built in MATLAB/Simulink 2021a to regulate the output and input between the solar array and electrolysis. Using the PID regulator, the error was determined as the difference between the reference set current and the output current.
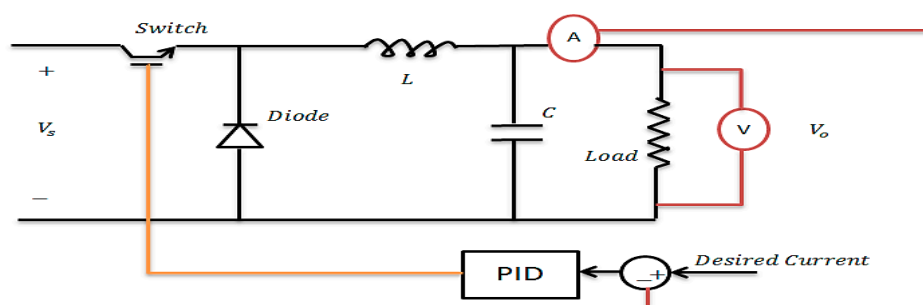
Figure 5. DC/DC Current Controlled Converter.

The buck converter has two modes: when the switch is turned on in the first mode of operation, the diode becomes reverse-biased, storing the provided energy in an inductance. When the switch is turned off in the second mode of operation, the diode becomes forward-biased owing to the output and it obtains energy from the inductance. The output is kept separate from the input [45].

Buck converters are utilized to manage the DC output voltage and current and to regulate the DC power source. The duty ratio (D) is the ratio of the time spent at ON mode to the periodic time. The duty ratio is also provided by the following equation [45]:

$$D = \frac{V_0}{V_s} = \frac{I_s}{I_0} \tag{5}$$

3.4. PEM Electrolysis

The PEM electrolysis mode refers to the process of reversing the flow of hydrogen into a fuel cell. Reversible voltage, activation overvoltage, ohmic potential, and diffusion over-potential (or concentration over-potential) are all included in the current–voltage (IV) equation [46,47]. In an electrolysis cell, the electrochemical process transforms DC electrical power into hydrogen to store energy in a chemical form. The electrical circuit of electrolysis is illustrated as a sensitive, nonlinear DC load, in which the greater the used voltage, the higher the input current flow and the more H_2 is produced. PEM electrolysis cells also have other benefits, such as being lighter, consuming less energy, and operating at lower temperatures. An electrical equivalent circuit for single-cell PEM electrolysis is depicted in Figure 6. It is implemented in a Simulink block diagram [42,48].
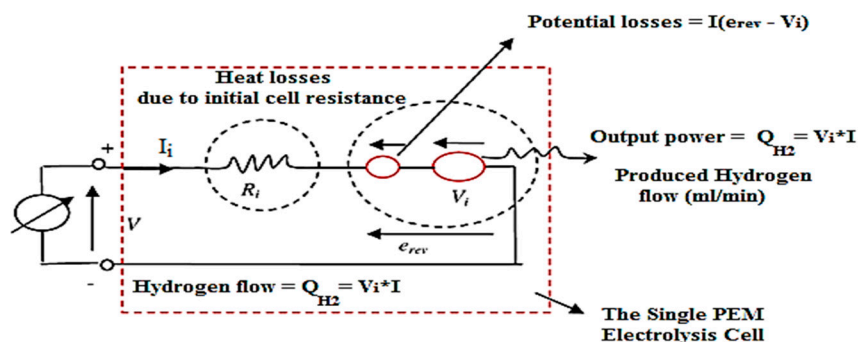

Figure 6. Equivalent electrical model for a single-cell PEM electrolysis.

Some equations for steady-state settings have been created and applied in MATLAB/Simulink to determine the I–V and hydrogen-generation characteristics. Equation (6), which is stated as follows, represents the electrolysis process in a steady-state operation [42]:

$$e_{rev} = V(p.T) - I_i R_i(P.T) \tag{6}$$

the ideal voltage, V_i, for the electrolysis is defined as following:

$$V_i = \frac{\Delta G}{2F} \qquad (7)$$

where ΔG is the Gibbs free energy charge of hydrogen gas and is provided by [44]:

$$\Delta G = 285.84 - 163.2(273 + t(°C)) \qquad (8)$$

The following equation can be used to compute the hydrogen generation rate (ml/min) as a function of $I(T.p)$ [45]:

$$Q_{H2} = \frac{60000 \, v_m I_i}{2F} \qquad (9)$$

where v_m is one mole volume calculated using the ideal gas equation:

$$v_m = \frac{R(273 + t(°C))}{p} \qquad (10)$$

The electrolytic input power is calculated based on Q_{H2} as:

$$P_{input} = VI_i = I_i^2 R_i + I_i e_{rev} = (\frac{2FQ_{H2}}{60000 v_m})^2 R_i + \left(\frac{2FQ_{H2}}{60000 v_m}\right) e_{rev} \qquad (11)$$

The output power, P_{H_2} (the electrochemical hydrogen energy per second), which correlates to hydrogen, is expressed as:

$$P_{H_2} = V_i I_i = \frac{\Delta G}{2F} * \frac{2FQ_{H2}}{60000 v_m} = \frac{\Delta G Q_{H2}}{60000 v_m} \qquad (12)$$

Finally, the efficiency of the PEM electrolysis can be expressed by:

$$\eta = \frac{P_{H_2}}{P_{input}} = \frac{V_i I_i}{VI_i} = \frac{V_i}{V} \qquad (13)$$

For a multi-celled PEM electrolysis with an n_p parallel and an n_s series design, the total input system voltage equation is expressed as:

$$V(p.T) = n_s e_{rev} + \frac{n_s}{n_p} I_i R_i(T.p) \qquad (14)$$

3.5. PEM Fuel-Cell Stack Modeling

The basic characteristics of the FC shown in Figure 7 can be categorized as input chemical energy, volume, and efficiency and can be formulated as in Equations (15)–(17), respectively [48,49].
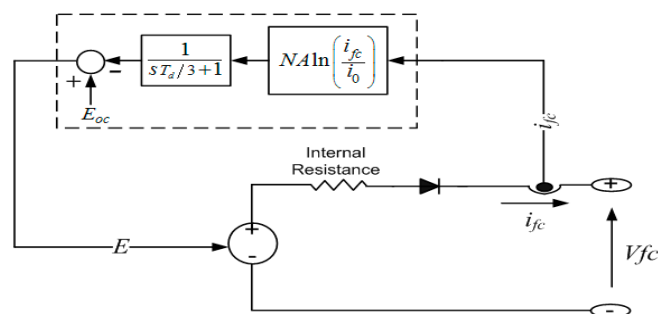
Figure 7. Electrical circuit equivalent circuit.

As n is the number of moles which can be calculated from the universal gas law, as follows:

$$n = \frac{P \times V}{R \times T} \tag{15}$$

$$\eta_{FC} = \frac{\text{Output Electrical Energy}}{\text{Input Chemical Energy}} = \frac{V_{FC\_nom} \times I_{FC\_nom} \times \text{Time}}{\left(\frac{\Delta h^o}{RT}\right) \times P_{Fuel} \times V_{Fuel} \times X\%} \tag{16}$$

$$V_{Fuel} = Q_{Fuel} \times \text{Time} \tag{17}$$

$$\eta_{FC} = \frac{V_{FC\_nom} \times I_{FC\_nom}}{\left(\frac{\Delta h^o}{RT}\right) \times Q_{Fuel} \times P_{Fuel} \times X\%} = \frac{60000 \times V_{FC\_nom} \times I_{FC\_nom}}{\left(\frac{\Delta h^o}{RT}\right) \times Q_{Fuel\_lpm} \times P_{Fuel} \times X\%} \tag{18}$$

The nominal rates of conversion (utilizations) for both hydrogen and oxygen are presented in Equations (19) and (20).

$$U_{F\_H_2} = \frac{60000 \times T \times R \times N \times I_{FC\_nom}}{F \times Z \times Q_{Fuel\_lpm} \times P_{Fuel} \times X\%} \tag{19}$$

$$U_{F\_O_2} = \frac{60000 \times R \times T \times N \times I_{FC\_nom}}{F \times 2Z \times Q_{Air\_lpm} \times P_{Air} \times Y\%} \tag{20}$$

The number of the cells in the stack is as follows in Equation (21):

$$N = \frac{Z \times F \times V_{FC\_nom} \times U_{F\_H_2}}{\eta_{FC} \times \Delta h^o} \tag{21}$$

The partial pressures for hydrogen, oxygen, and water vapor are derived in Equations (22)–(24), respectively [48].

$$P_{H_2} = \left(1 - U_{F\_H_2}\right) \times P_{Fuel} \times X\% \tag{22}$$

$$P_{O_2} = \left(1 - U_{F\_O_2}\right) \times P_{Air} \times Y\% \tag{23}$$

$$P_{H_2O} = \left(W + 2 \times Y\% \times U_{F\_O_2}\right) \times P_{Air} \tag{24}$$

The Nernst voltage for the fuel cell is developed in either Equation (25) or Equation (26) [48]:

If the temperature (T < 100):

$$E_n = 1.229 - \left\{ (T - 298)\frac{44.43}{Z \times F} \right\} + \left\{ \frac{R \times T}{Z \times F} \ln\left[P_{H_2}\sqrt{P_{O_2}} \right] \right\} \tag{25}$$

If the temperature (T > 100):

$$E_n = 1.229 - \left\{ (T - 298)\frac{44.43}{Z \times F} \right\} + \left\{ \frac{R \times T}{Z \times F} \ln\left[\frac{P_{H_2}\sqrt{P_{O_2}}}{P_{H_2O}} \right] \right\} \tag{26}$$

Therefore, the electrical circuit parameters can be presented as follows:

(i) Open-Circuit Voltage—voltage at zero current:

$$E_{O.C.} = K_c * E_n \tag{27}$$

(ii) Exchange Current—a reverse-saturation current, which is a very small current opposite the mainstream current, I_FC:

$$I_o = \frac{Z \times F \times K \times \left(P_{H_2} + P_{O_2}\right)}{R \times h} \exp(\frac{-\Delta G}{R \times T}) \tag{28}$$

(iii) Gibbs Energy—a thermodynamic energy:

$$\Delta G = K_G \times Z \times E_n \tag{29}$$

(iv) Tafel Slope (A)—the slope of the ohmic region:

$$A = \frac{R \times T}{Z \times F \times \alpha} \tag{30}$$

Eventually, the electric model of the stack can be derived in Equations (31) and (32).

$$V_{FC} = E - I_{FC} \times R_S \tag{31}$$

$$E = E_{O.C.} - NA\ln\left(\frac{I_{FC}}{I_O}\right) \tag{32}$$

A fuel cell PEMFC stack (Fuel Cells ETc Company), illustrated in [49], consists of 42 cells in series with a power capacity of 1.26 KW and a nominal voltage of 24.23 V$_{dc}$.

All the above equations, from (15) to (32), were simulated to develop a premium, valid FC model which has been characterized by voltage—current and power—current curves, as indicated in Figure 8 [48].
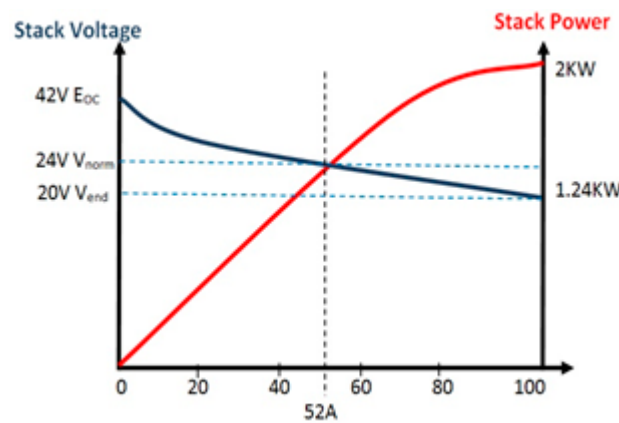

Figure 8. Voltage—current and power—current fuel cells' stack characteristics.

3.6. Hydrogen Tank Modeling

Figure 9 depicts a schematic representation of a hydrogen storage tank during fueling.
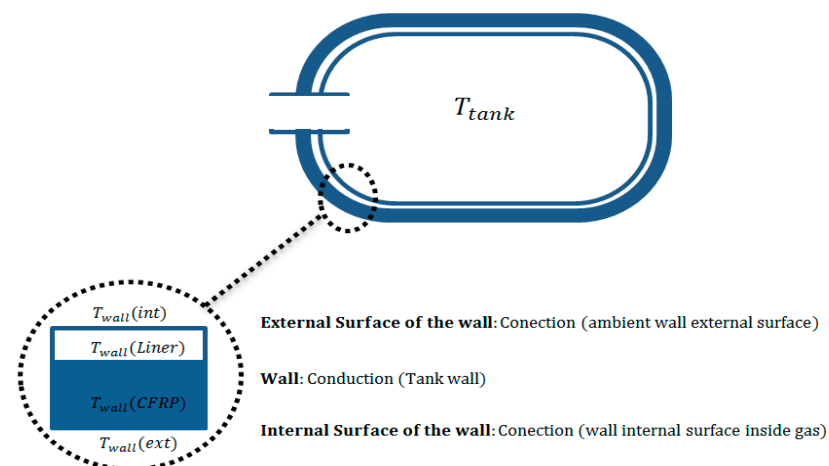

Figure 9. Hydrogen tank.

The following equation is used to compute the thermodynamic properties of hydrogen during the fueling process:

$$\Delta P = \frac{z N_{H_2} R T_m}{M_{H_2} V_T} \tag{33}$$

$$\Delta P = P_{measured} - P_{initial} \tag{34}$$

3.7. Proposed Double Stage Boost Converter Model

This research used a high-efficiency, two-stage boost converter proposed by the authors because an inverter integrated with a double-stage boost converter can control the dead time of the next voltage source inverter, reducing it to 63.01 μs. This is in comparison to the 180.02 μs dead time offered by traditional methods [50]. The main circuit of the suggested converter is shown in Figure 10. The converter can be described as double-boost converters cascaded together. The transistors in this model are considered to be ideal. The load can be cosidered resistive by adjusting the output voltage to avery low-ripple DC voltage so that any series inductance can be converted to a short circuit. The input voltage is immediate and continuous. The stages of the converter are intendeded to function in a continuous conduction mode. The second stage consists of loading the first stage. In the case of the large-size motor, the load resistance of the second stage is 35.446 ohm, and the load resistance of first stage is 2.041 ohm.
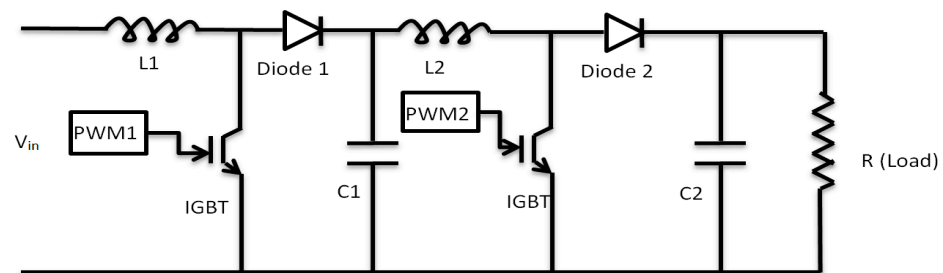

Figure 10. The circuit diagram of a double-stage boost converter.

As the suggested boost converter has two stages, Equation (35) can be used to obtain the voltage conversion ratio:

$$M(D) = \frac{V_0}{V_i} = \left(\frac{1}{1 - D_1}\right)\left(\frac{1}{1 - D_2}\right) \tag{35}$$

The inductance and capacitance of each stage can be estimated as [50]:

$$L_{min} = \frac{V_{in}(V_o - V_{in})}{\Delta I_L f_s V_o} \tag{36}$$

$$C_{min} = \frac{V_o D}{R \Delta V_o f_s} \tag{37}$$

The duty ratios for the first stage and second stage are D_1 and D_2, respectively. The duty cycles of both stages can be calculated by knowing the output range and input voltage for specific appliances; the specifications for the proposed double-stage boost converter are shown in Tables 3 and 4.

Table 3. Specifications of the first stage.

| Parameters	Value
Voltage at the input end, V_{in}	42.0 V
Voltage at the output end, V_o	175.0 V
Duty cycle, D_1	0.758
Switching frequency, f_s	20.0 KHz
Resistance, R	2.041 Ω
Minimum inductance, L_{min}	43.776 mH
Capacitance, C_{min}	18.89 μF
Current of inductor, I_L	10.42 A

Table 4. Specifications of the second stage.

Parameters	Value
Voltage at the input end, V_{in}	175.0 V
Voltage at the output end, V_o	729.1725 V
Duty cycle, D_1	0.758
Switching frequency, f_s	20.0 KHz
Resistance, R	35.446 Ω
Minimum inductance, L_{min}	6.78 mH
Capacitance, C_{min}	1.74 μF
Current of inductor, I_L	2.404 A

3.8. Indirect Rotor Field-Oriented Control (IRFOC)

The induction machine regulated by indirect rotor field-oriented control has a rotor flux aligned with the d-axis and the electromagnetic-developed torque aligned with the q-axis. An analysis of the current, voltage, and flux of the motor in terms of a space vector is possible, as in Equation (38). A decoupled control of the torque and flux quantities can be achieved by orienting the RRF on the stator flux, rotor flux, or air-gap flux [51]. In this note, rotor field-oriented control (RFOC) was chosen for its simplicity and higher torque dynamics [51].

$$i_s = i_a + i_b e^{j\frac{2\pi}{3}} + i_c e^{j\frac{4\pi}{3}} \tag{38}$$

where (a, b, c) are the three-phase system domain, which must be converted into a two-time variant coordinate system. Using a conversion matrix, we first transform (a, b, c) into (α, β) and then convert (α, β) into (d, q). The conversion matrix for transforming (a, b, c) into (α, β) is given in Equation (39). The conversion matrix for transforming (α, β) into (d, q) can be found in Equation (40). Figure 11 shows the relationship between the two domains.
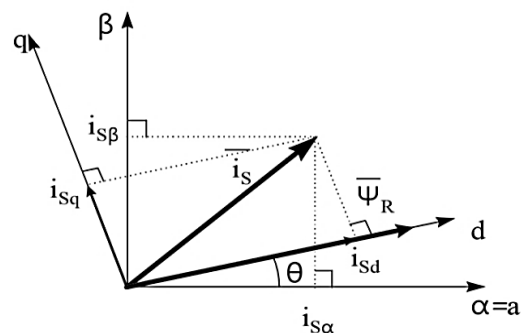
Figure 11. Stator-current vector and its components in the (α, β) and (d, q) domains.

$$i_{\alpha\beta o} = \frac{2}{3} * \begin{bmatrix} 1 & -\dfrac{1}{2} & -\dfrac{1}{2} \\ 0 & \dfrac{\sqrt{3}}{2} & -\dfrac{\sqrt{3}}{2} \\ \dfrac{1}{2} & \dfrac{1}{2} & \dfrac{1}{2} \end{bmatrix} \tag{39}$$

$$i_{dqo} = \frac{2}{3} * \begin{bmatrix} cos\theta & \cos\left(\theta - \dfrac{2\pi}{3}\right) & \cos\left(\theta + \dfrac{2\pi}{3}\right) \\ sin\theta & \sin\left(\theta - \dfrac{2\pi}{3}\right) & \sin\left(\theta + \dfrac{2\pi}{3}\right) \\ \dfrac{1}{2} & \dfrac{1}{2} & \dfrac{1}{2} \end{bmatrix} \tag{40}$$

where θ is the direction of the rotor flux. The flux and torque current components are estimated by the following formulas:

$$i_{sd} = i_{s\alpha}cos\theta + i_{s\beta}sin\theta \qquad (41)$$

$$i_{sq} = -i_{s\alpha}sin\theta + i_{s\beta}cos\theta \qquad (42)$$

These values rely on the current vector (α, β) components and on the flux position in the rotor; if the flux position can be determined exactly using a position sensor, the d and q components can then be estimated by this projection [52].
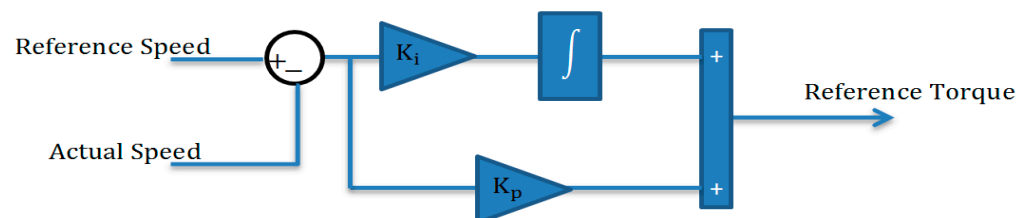
3.9. Speed Regulator

3.9.1. Proportional Integral Regulator

The control law for this technique is as follows:

$$\text{T} = K_p * e + K_i * \int e \, dt \qquad (43)$$

$$e = \omega^* - \omega \qquad (44)$$

where ω and ω^* are the actual and reference speeds, respectively. The controller output is controlled by the PI speed regulator gains (K_p and K_i) that follow a set of principles to provide optimum control performance, even when parameter volatility and drive nonlinearity are present. The high value of the error is amplified across the PI regulator in starting mode, resulting in considerable variances in the required torque. If the K_p and K_i values of the PI speed regulator surpass a specific threshold, the required torque fluctuates too much, destabilizing the system. To solve this problem, a limiter is used after the PI regulator. When properly adjusted, this limiter keeps the speed error within limits, resulting in smooth variations in the necessary torque even when the gains from the PI speed regulator are relatively significant [53–55]. Figure 12 shows the block diagram for the PI controller. The K_p and K_i values of the PI speed regulator have been estimated using particle swarm optimization.

Figure 12. Simulation design of a PI speed regulator.

3.9.2. Fuzzy PID

It was discovered that the fuzzy PID technique is substantially more efficient. The fuzzy-PID technique non-linearizes with the individual's expertise and expert knowledge of the process to be regulated while constructing the regulator. When compared to traditional linear regulators, this method improves the performance, dependability, and resilience of the system [54–56]. Figure 13 depicts the block diagram model of a fuzzy PID speed regulator. This regulator model is simulated using a Sugeno-type fuzzy inference system (FIS) with two inputs, the error "e" in Equation (44) and the change in error "Δe" in Equation (45), and one output, (T_e^*). The K_p, K_d, and K_o values of the fuzzy PID speed regulator have been estimated using C-BO, and the output results have been compared to the parameters estimated using PSO.
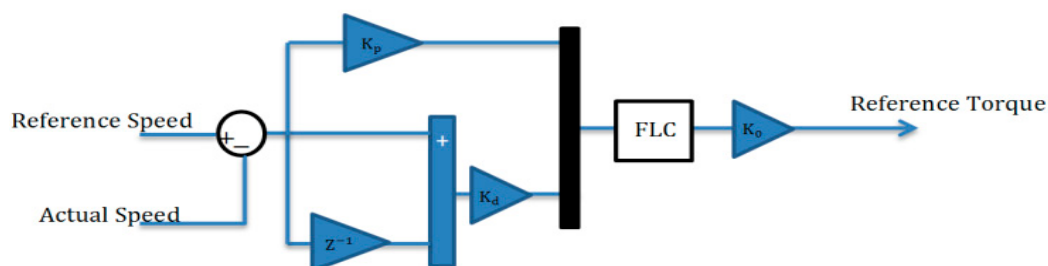
$$\Delta e = e_k - e_{k-1} \qquad (45)$$

Figure 13. Block diagram of fuzzy PID speed regulator.

The memberships of every input and output are shown in Figure 14. The rules to obtain the values of the desired torque are described in Table 5.
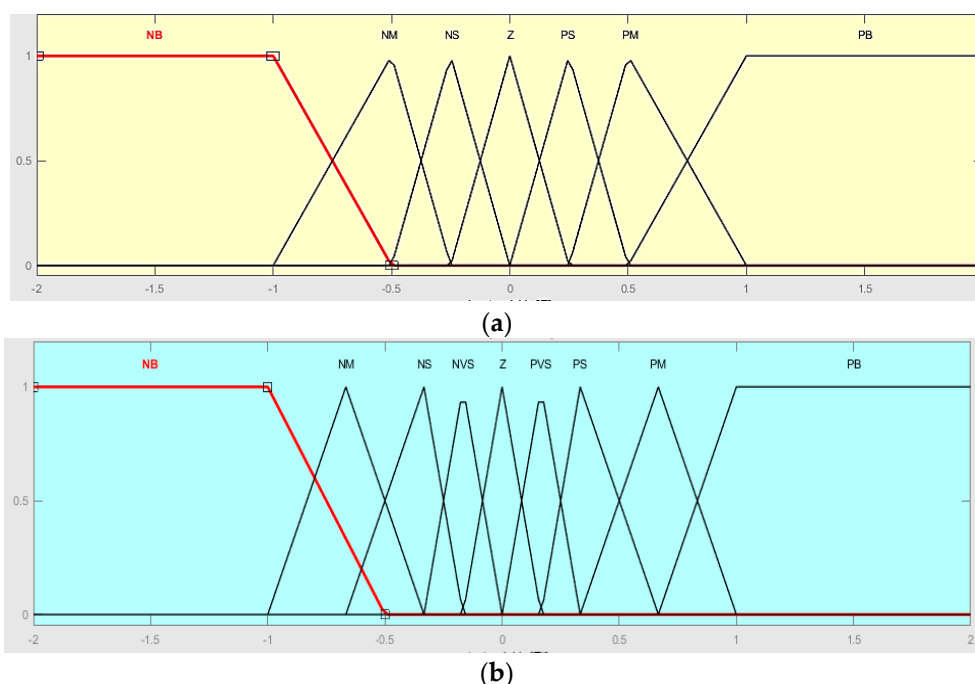

(**a**)

(**b**)

Figure 14. Membership functions for (**a**) error and change in error, and (**b**) output.

Table 5. Rule base for fuzzy logic, controller-based induction motor drive.

e Δe	NB	NM	NS	Z	PS	PM	PB
NB	NB	NB	NB	NM	NS	NVS	Z
NM	NB	NB	NM	NS	NVS	Z	PVS
NS	NB	NM	NS	NVS	Z	PVS	PS
Z	NM	NS	NVS	Z	PVS	PS	PM
PS	NS	NVS	Z	PVS	PS	PM	PB
PM	NVS	Z	PVS	PS	PM	PB	PB
PB	Z	PVS	PS	PM	PB	PB	PB

4. C-BO Technique

4.1. Billiards Optimization Approach

The complex structure of the present industrial systems has given rise to a variety of metaheuristic algorithms that have been developed to discover the best solutions. The BOA optimization technique was influenced by the well-known game of pool [34,57]. Balls are struck with a cue and then passed around a table in the game of billiards. Billiards

is played on a table with six pockets: one in each corner and two along each long side. The player advances a cue ball in the direction of the balls to smash them. The player then needs to move the balls into better positions. A potential solution in the BOA is depicted as a multi-dimensional pool ball made up of several decision-making criteria. The two types of balls are normal balls and cue balls. The cue ball strikes a target ball, forcing it into a corner. Kinematic and collision laws are generated as a result of ball contact. The BOA optimization procedure is demonstrated in the following.

(a) Initialization**:** the initial distribution of the balls' space agents is as follows:

$$B_{n.m}^0 = Var_m^{min} + randam_{[0.1]}(Var_m^{max} - Var_m^{min}) \tag{46}$$

$$n = 1.2.3 \dots .2N; \qquad m = 1.2.3 \dots .M$$

where $random_{[0.1]}$ represents a randomly chosen number that occurs equally between [0, 1]. Variable numbers and populations are indicated by M and 2N.

(b) Identification: the placements of the ball and pocket are used to evaluate objective functions;

(c) Pocket determination: the pocket of this algorithm plays two roles: (i) a ball objective, which offers the ability of the algorithm to utilize, and (ii) memory, which keeps track of the first highest solutions discovered. The goal of this memory is to enhance the BOA's performance without raising the cost of computation. Each cycle updates the ideal ball positions using this memory;

(d) Grouping the balls: the balls are grouped based on how accurate they are. The two types of balls are normal balls and cue balls. The first sets of those balls are normal balls (i.e: $n = 1.2. \dots . N$), and the second set are cue balls (i.e., $n = N + 1. \dots . 2N$). In an exceptional group, every cue ball has the same rank [34];

(e) Giving a destination pocket to balls: each ordinal ball is provided with a destination pocket by selection using a roulette wheel. In the pockets, more features are promised in exchange for a lower fitness value. The chance of being mugged is as follows:

$$P_K = \frac{e^{-\beta fk}}{\sum_k e^{-\beta fk}} ; k = 1.2.3 \dots . k \tag{47}$$

The cue balls make contact with the target balls, which then fall into the pockets;

(f) Ball-location updating: after the collision, the new locations of the normal balls are updated. The next positions for normal balls are as follows:

$$PR = \frac{iter}{iter_{max}} \tag{48}$$

$$B_{n.m}^{new} = rand_{[-ER.ER]}(1 - PR)(B_{n.m}^{old} - P_{k.m}^n) + P_{k.m}^n , \qquad n = 1,2,3, \dots N \tag{49}$$

where the accuracy rate is clarified by PR. Following the collision, the positions of the cue balls are determined by their speeds, which are computed as following:

$$\vec{v_n} = sqrt(2a\overrightarrow{B_n^{old}B_n^{new}})\widehat{B_n^{old}B_n^{new}} \tag{50}$$

Cue ball velocities are determined as following:

$$\overrightarrow{v_{n+N}} = \frac{\overrightarrow{v'_n}}{B_n^{\widehat{old}B_n^{new}} . B_{n+N}^{old} + NB_n^{old}} B_{n+N}^{old} \widehat{B_n^{old}}; n = 1,2,3, \dots N \tag{51}$$

$$\overrightarrow{v'_{n+N}} = \omega(1 - \frac{iter}{iter_{max}})(\overrightarrow{v_{n+N}} - \overrightarrow{v'_n}) \tag{52}$$

where ω designates a predetermined number [0, 1] for regulating the movement of the cue ball. The following equations are the updated cue ball position:

$$\overrightarrow{B_{n+N}^{new}} = \frac{\overrightarrow{v'_{n+N}}}{2a} \overrightarrow{v'_{n+N}} + \overrightarrow{B_n^{old}} \quad n = 1,2,3 \dots . N \tag{53}$$

(g) Testing the limits of the boundary conditions: the final ball placements may be beyond the desired range as a result of balls falling out of the table when their locations are updated. As a result, the size of the balls need to be adjusted;

(h) Examining the termination circumstances: the process will be finished once certain requirements, such as the total number of iterations, have been satisfied. If the requirements are not met, the process will continue.

4.2. Chaotic Billiards Optimization Approach

We selected the innovative (C-BO) algorithm over PSO because its formulation is clear and easy to apply. Due to the superior performance of the PSO in prior optimization attempts, PSO was chosen as the best competing challenge for C-BO because PSO has the best global union and demonstrates a very good implementation ease and very good merge speed when compared to other optimization algorithms [31,58–61]. The process of initialization in the billiards optimization approach is performed randomly because of the population sample selection as in (46), and therefore cannot achieve an accurate beginning procedure. Due to the fact that metaheuristic approaches are highly sensitive to initial states, appropriate starting states will improve the performances of these approaches. The major significance of merging chaotic with metaheuristic approaches and examining their effect on performance is demonstrated in [62,63]. CLM are the greatest alternative because of their increased processing efficiency. Additionally, logistic maps have a better likelihood of obtaining values between 0 and 1, enabling quicker local searches. This chaotic map has the formula:

$$y_1 = rank$$

$$y_{s+1} = 4.y_s(1 - y_s). \quad s = 1.2. \dots \tag{54}$$

This selection is performed instead of the initialization process of the BOA in step (a) presented in Equation (46), in which the rank is a matrix of random integral numbers in the range of [0, 1]. The C-BO algorithm was built by replacing the value of $random_{[0.1]}$ with the CLM vector (54). The traditional BOA can be strengthened and improved with a chaotic character, thus showing much better-distributed solutions and a better quality of the solutions.

5. Tuning Parameters and Simulation Process

In this section, C-BO is used to select the optimal coefficients K_P, K_d, and K_o of the speed regulator mentioned in Figure 13. The optimization process is an offline optimization under the varying mechanical loading and solar irradiance with a convergence rate shown in Figure 15. The chaotic billiards optimization is achieved using 40 agents and 300 iteratives. Figure 16 depicts the ISE fitness-function convergence of the C-BO, which demonstrates a lower change after 300 iterations. The C-BO found the optimal solution in 11 s using the lower value of the ISE. In particular, the C-BO technique converges more rapidly than the PSO. The parameters of the optimal controllers are shown in Table 6 for

both the 20 HP and 2.5 HP induction motors under a desired speed of 50 rad/s. As a result, the control input forces the system to produce an output that is as close as feasible to the position that was planned. In this method, the conventional BOA with a chaotic character can be reinforced and enhanced to display considerably more distributed solutions with better quality. Figure 15 shows that the C-BO converged faster. Hence C-BO is efficient, robust, and capable of handling mixed-integer, nonlinear optimization problems.
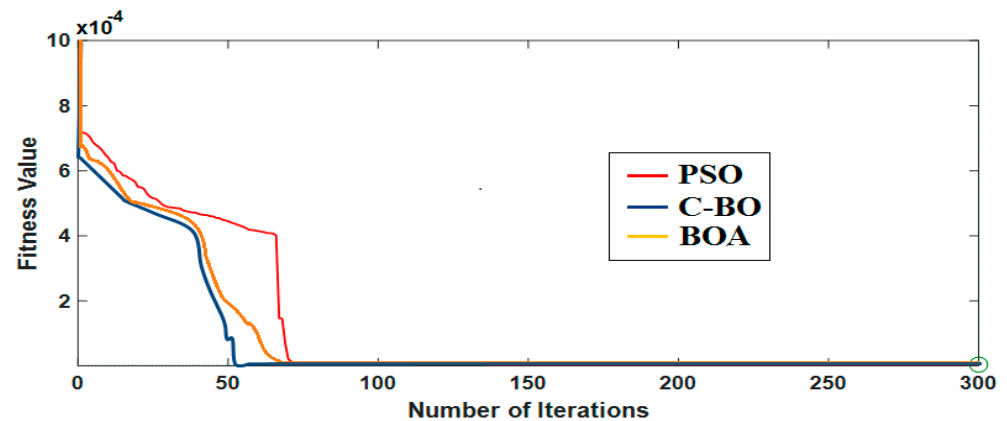

Figure 15. Cost convergence for fuzzy PID over iterations.

Table 6. Optimal parameters of the speed regulator.

Technique	Induction Motor Size	Parameters
PI speed regulators optimized with PSO	20 HP	Kp = 50.679
		Ki = 40.250
	2.5 HP	Kp = 48.36
		Ki = 36.253
Fuzzy PID speed regulators optimized with C-BO	20 HP	Kp = 30.2
		Kd = 40.1
		Ko = 100.32
	2.5 HP	Kp = 29.12
		Kd = 39.21
		Ko = 98.61
Fuzzy PID speed regulators optimized with PSO	20 HP	Kp = 28.43
		Kd = 38.43
		Ko = 103.5
	2.5 HP	Kp = 26.15
		Kd = 37.69
		Ko = 101.96

6. Simulation Setup

Simulation was achieved by creating each section independently in the MATLAB/Simulink environment, as is shown in Figure 2, allowing the error to be easily tracked and the simulation blocks to be debugged. Each machine block was introduced and tested to ensure that it was capable of carrying out the simulation and providing appropriate results. PV solar panels, a DC/DC buck converter, and electrolysis were all designed to work together as modules. Several scenarios can be represented via simulation.

7. Simulation Results

To investigate the behavior of the studied control techniques, the simulation was performed on two different induction motors (a large-scale induction motor and a small-scale

induction motor). The large-scale induction motor was investigated with the PI-based PSO regulator; fuzzy-PID-based PSO; and a fuzzy-PID-based C-BO using Matlab/Simulink 2021a in Section 7.1. The small-scale induction motor was investigated in Section 7.2. The hydrogen results are summarized in Section 7.3.

7.1. Large-Size Induction Motor

The simulation model first needed to be initialized in order to obtain all of the parameters of the machine. The induction motor used here was a two-pole, 20 HP, 400 V, and 50 Hz motor. For each model, the rotor speed was measured for 2 s. At 1000 W/m², 1 atm, and 20 °C, the results of the output speed under no load utilizing a PI-based PSO regulator, a fuzzy-PID-based PSO, and a fuzzy-PID-based C-BO are displayed. Table 7 and Figure 16 show the dynamic characteristics of different mechanical loads (0 Nm, 25 Nm, and 50 Nm). For example: with no load, the overshoot peak value of speed using the PI-based PSO was 9.1 rad/s, while it was 5.3 rad/s with the fuzzy-PID-based PSO and 2.9 rad/s with the fuzzy-PID-based C-BO. The proposed fuzzy-PID-based C-BO speed regulator had a 6.1% faster speed-rising time than the fuzzy-PID-based PSO and a 9.5% faster speed-rising time than the PI–PSO speed controller, as well as demonstrating an excellent dynamic responsiveness value when compared to the other speed regulators.
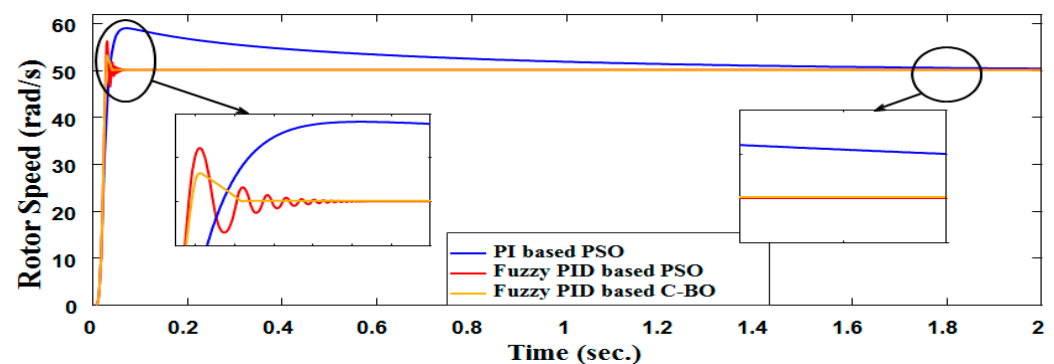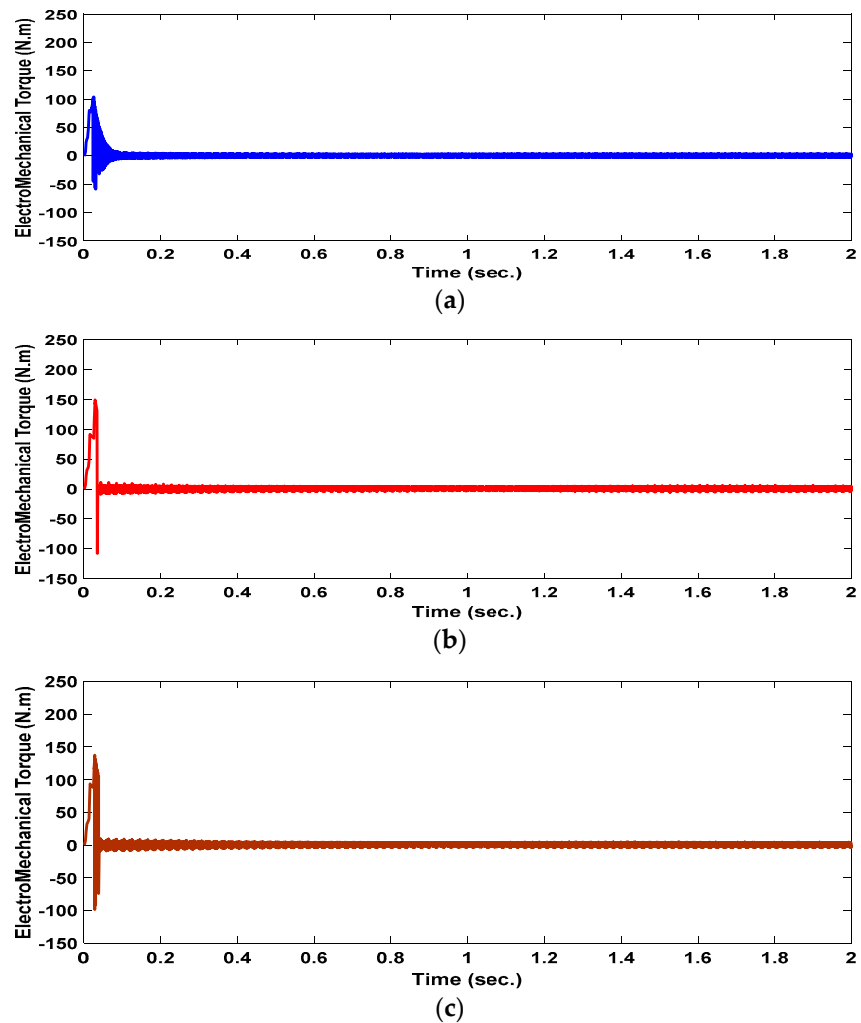

Figure 16. The rotor speed for the desired speed, 50 rad/s, at zero load.

**Table 7.** Speed controller performances at different loading values, 1000 W/m², 1 Atm, and 20 °C.

Load (N.m)	Type	Tr (ms)	Tp (s)	Mp (%)	Steady-state Error (%)
0	PI-based PSO	31.05	0.049	9.1	±0.85
	Fuzzy-PID-based PSO	29.55	0.040	5.3	±0.07
	Fuzzy-PID-based C-BO	28.08	0.040	2.9	±0.05
25	PI-based PSO	26.15	0.054	6.6	±0.9
	Fuzzy-PID-based PSO	25.98	0.043	4.44	±0.07
	Fuzzy-PID-based C-BO	24.97	0.043	2.00	±0.05
50	PI-based PSO	25.40	0.057	6.1	±1
	Fuzzy-PID-based PSO	24.90	0.046	3.8	±0.07
	Fuzzy-PID-based C-BO	23.85	0.046	2.2	±0.02

Figure 17 shows how the fuzzy-PID-based C-BO resulted in less torque ripple but a large bounce between positive and negative at the transient; this will cause a lower settling time and peak overshoot. Using a PI-based PSO and a fuzzy-PID-based C-BO will result in faster torque settling than using a fuzzy-PID-based PSO. Note that the fuzzy-PID-based PSO type resulted in a non-periodic steady-state ripple.

Figure 17. The motor-developed torque for the desired speed of 50 rad/s at zero load for a (**a**) PI-based PSO, (**b**) fuzzy PID based PSO, and (**c**) fuzzy-PID-based C-BO.

Figure 18 shows the line current for phase A for each method of control (PI-based PSO; the fuzzy-PID-based PSO; and the fuzzy-PID-based C-BO). The fuzzy-PID-based C-BO approach had the lowest transient ripple current. Fuzzy-PID-based C-BO has a reduced transient time and has a 6.1% faster speed-rising time than the fuzzy-PID-based PSO and a 9.5% faster speed-rising time than the PI–PSO speed controller.
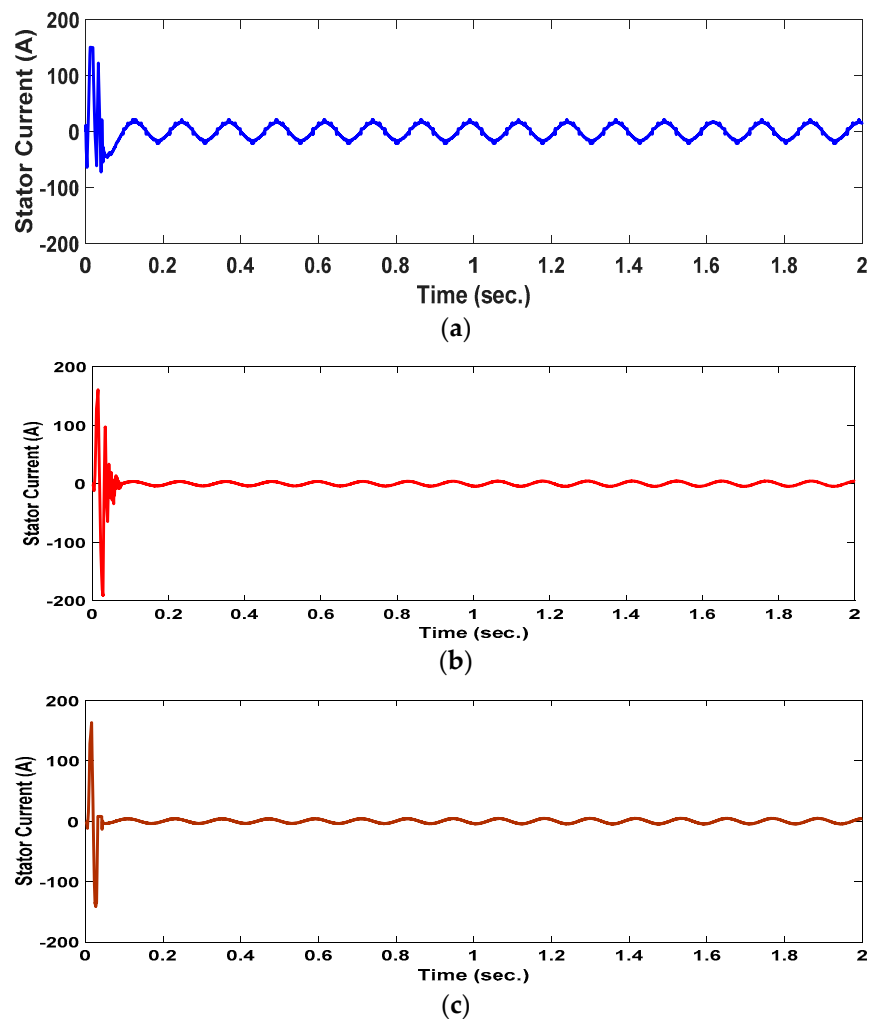
Figure 18. The stator current for the desired speed of 50 rad/s at zero load for the (**a**) PI-based PSO, (**b**) PSO with fuzzy PID, and (**c**) fuzzy-PID-based C-BO.

To ensure that the fuzzy-PID-based C-BO would work for the majority of the runs, the average of the optimized steady-state speed error and the corresponding standard deviation for forty independent runs were generated, displayed, and compared as illustrated for the PI-based PSO speed regulator, fuzzy-PID-based PSO, and the fuzzy-PID-based C-BO, as is shown in Table 8. In the case of the fuzzy-PID-based C-BO, the average steady-state speed error was reduced by 94.6% when compared to the PI-based PSO and 43.1% when compared to the fuzzy-PID-based PSO.

Table 8. Comparison of statistical results.

Technique	Ave.	Std. dev.
Using PI-based PSO	0.814	0.0435
Using fuzzy-PID based PSO	0.0764	0.0052
Using fuzzy-PID-based C-BO	0.0435	0.0042

7.2. Small Size Induction Motor

The induction motor used here was a 6-pole, 1.8 kW, 380 V, and 50 Hz motor. For each model, the rotor speed was measured for 5 s. At 1000 W/m², 1 atom, and 20 °C, the results of the output speed under no load utilizing the fuzzy-PID-based PSO, and the fuzzy-PID-based C-BO are displayed. The proposed induction motor was subjected to a load torque, as is shown in Figure 19. From t = 0 s to t = 1 s, the motor was subjected to

zero torque. At t = 1 s, the load torque increased suddenly to 3 N.m. At t = 2 s, the load torque suddenly stepped up to 5 Nm. At t = 3 s, the load suddenly stepped down to 4 N.m.
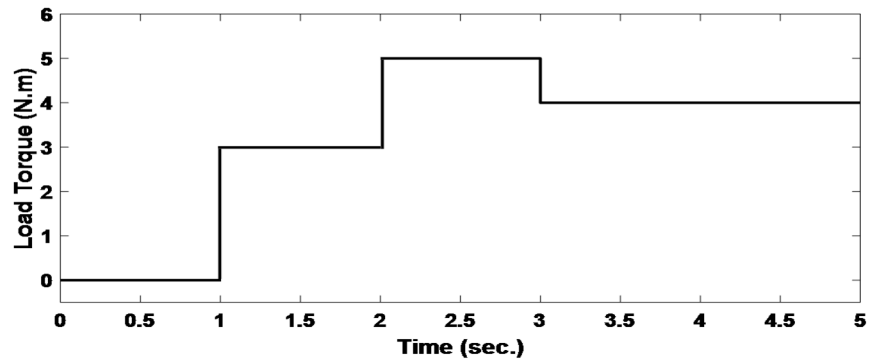

Figure 19. Proposed load torque.

The rotational speeds under the fuzzy-PID-based PSO and fuzzy-PID-based C-BO are shown in Figure 20. When compared to the fuzzy-PID-based PSO, fuzzy-PID-based C-BO had a lower peak overshoot, a less transient ripple, shorter rising and settling times, and was less affected by load variation. The overshoot peak value of speed using fuzzy-PID-based PSO was 9.1 rad/s, while it was 0.9 rad/s with fuzzy-PID-based C-BO. At t = 1 s and t = 2 s, the fuzzy-PID-based PSO had a higher steady error than the fuzzy-PID-based C-BO due to an increase in loading. At t = 3 s, the speed of the fuzzy-PID-based PSO had a higher peak overshoot than the speed of the fuzzy-PID-based C-BO due to a sudden reduction in loading.
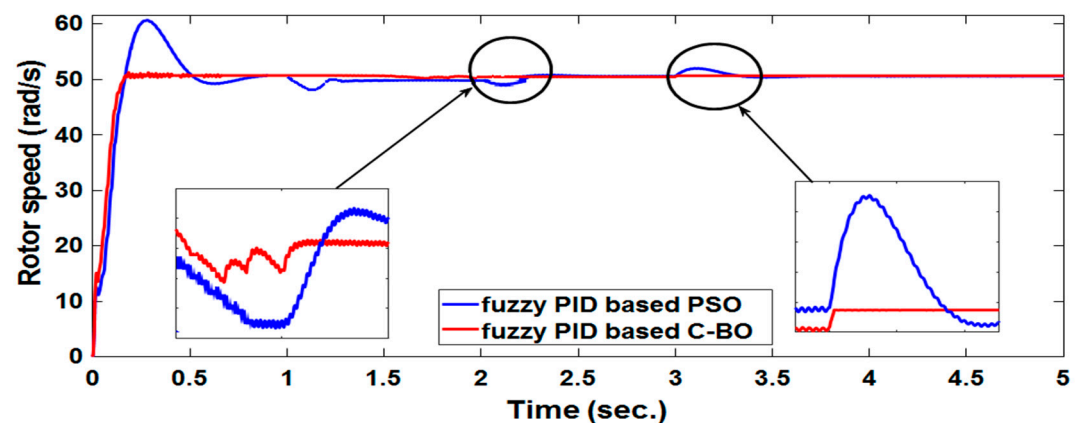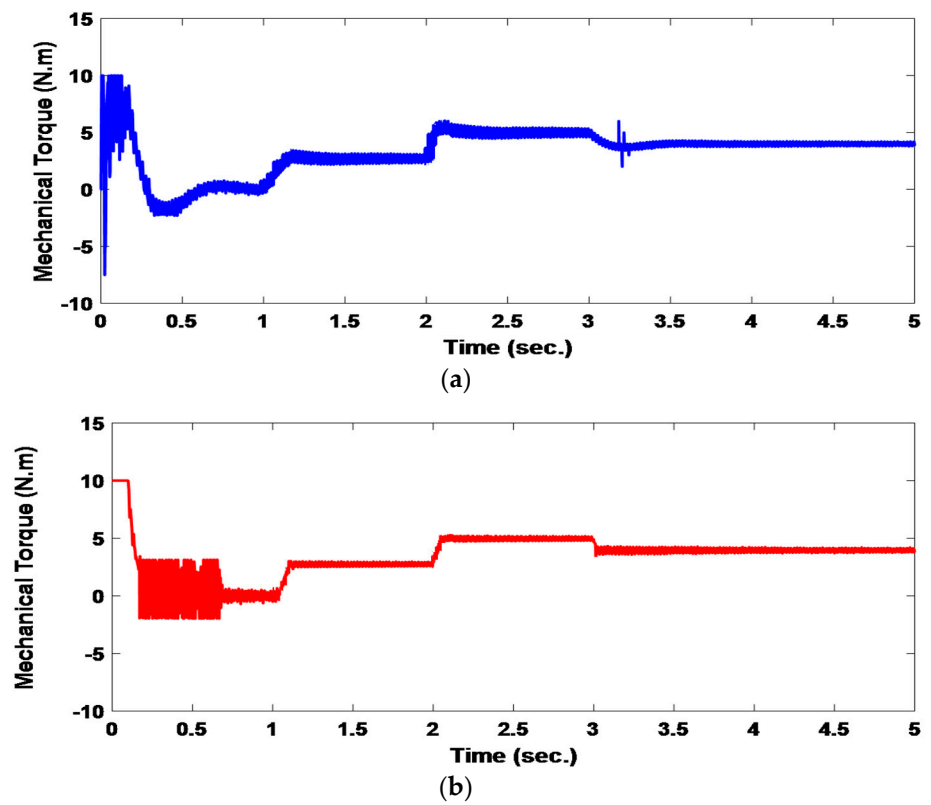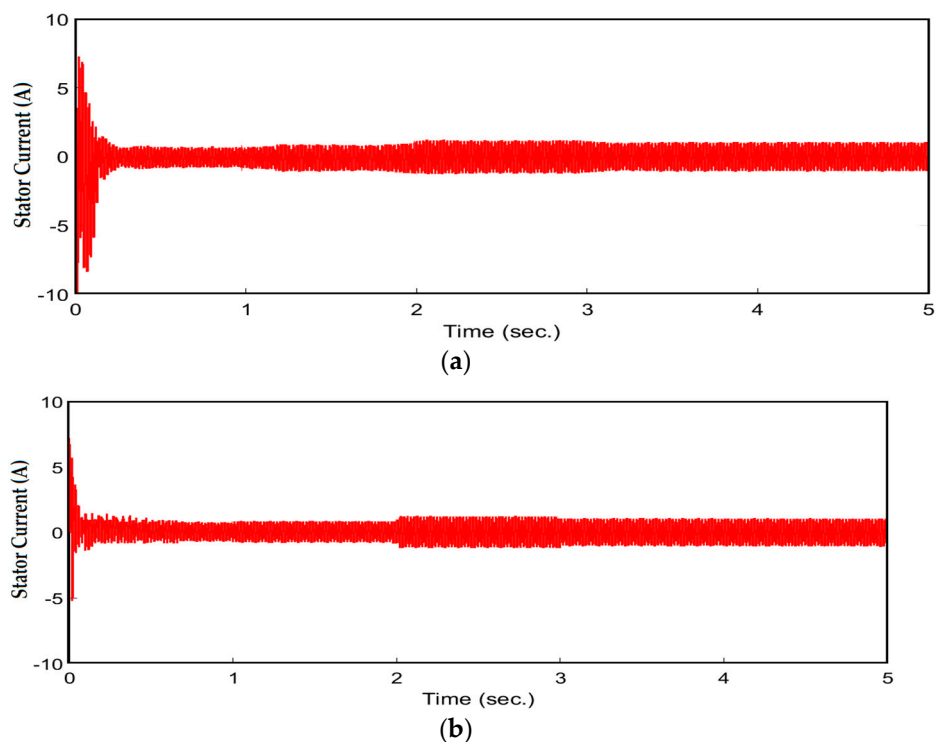

Figure 20. The motor speed for the desired speed, 50 rad/s.

Figure 21 shows the experimental findings of mechanically developed torque under the fuzzy-PID-based PSO and an fuzzy-PID-based C-BO. The fuzzy-PID-based C-BO had the disadvantage of having a larger transient ripple when the motor started from zero speed, but it performed better under a steady state and load change. By using fuzzy-PID-based C-BO, the mechanical torque tracking was improved by 65% when compared to use of the fuzzy-PID-based PSO for the small induction motor.

(a)

(b)

Figure 21. The motor-developed torque for the desired speed, 50 rad/s, for (**a**) fuzzy PID based PSO and (**b**) fuzzy-PID-based C-BO.

Figure 22 describes the results of the Phase A stator current using PSO with fuzzy PID and fuzzy-PID-based C-BO. It is noted   that the fuzzy-PID-based C-BO had   reduced in-rush energy losses by a 67.32% response when the motor started from zero speed. It also demonstrated a better performance under steady-state and load variation.


(a)

(b)

Figure 22. The Stator current for the desired speed, 50 rad/s, for (**a**) fuzzy PID based PSO and (**b**) fuzzy-PID-based C-BO.

7.3. Hydrogen Production

The PV panel in this study employed MPPT to deliver the maximum power, while the electrolysis used a DC/DC current source converter to provide the highest hydrogen output. Figure 23 depicts the flow rate of hydrogen (mL/min) vs. the current (A). It is worth noting that the relationship between the flow rate of hydrogen and the input current is linear. Figure 24 shows the flow rate of hydrogen (mL/min) vs. the input power (watts). It is worth noting that, as the power level grew, so did hydrogen production. The efficiency of PEM electrolysis as a function of input power is depicted in Figure 25. As can be seen in Equation (13), as the input voltage increased, the efficiency decreased. The efficiency of the system fell exponentially as the input power increased. Figure 26 shows the pressure inside the hydrogen tank model at 1 atmosphere and 20 degrees Celsius, 4 atmosphere and 20 degrees Celsius, and 1 atmosphere and 60 degrees Celsius. With the passage of time, the amount of hydrogen increased.
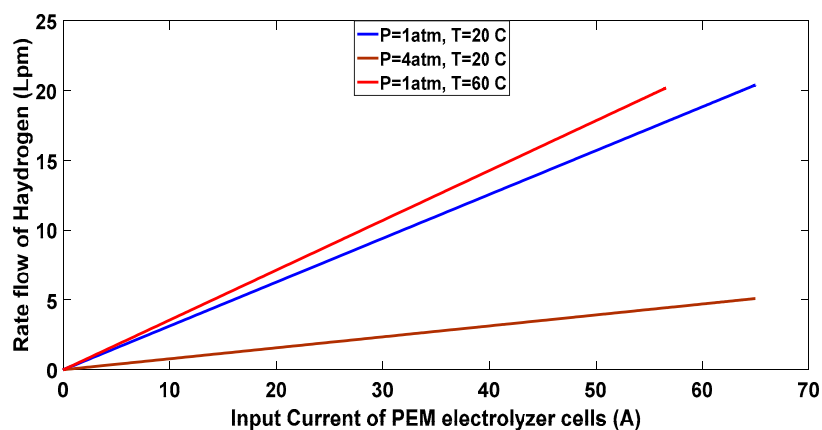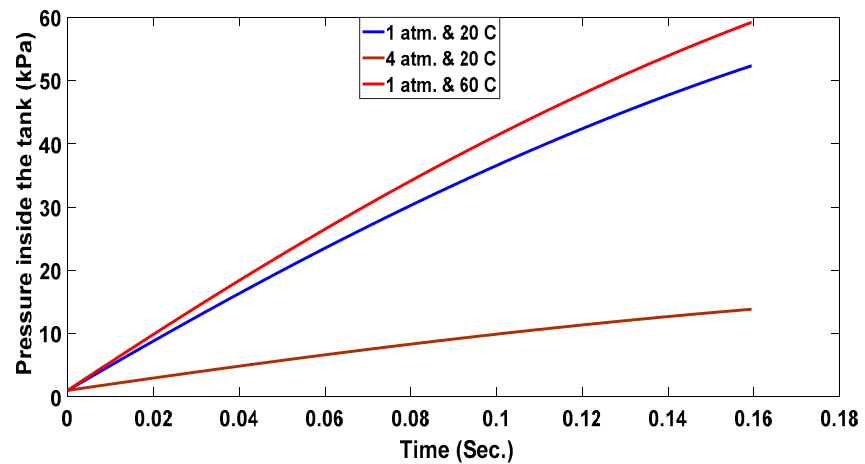

Figure 23. Flow rate of hydrogen vs. input current of PEM electrolyzer at different operating conditions.
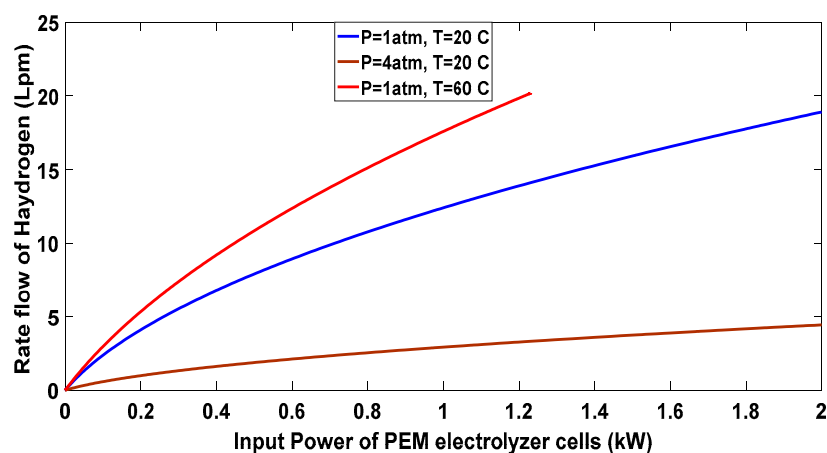
Figure 24. Flow rate of hydrogen vs. input power of PEM electrolyzer at different operating conditions.
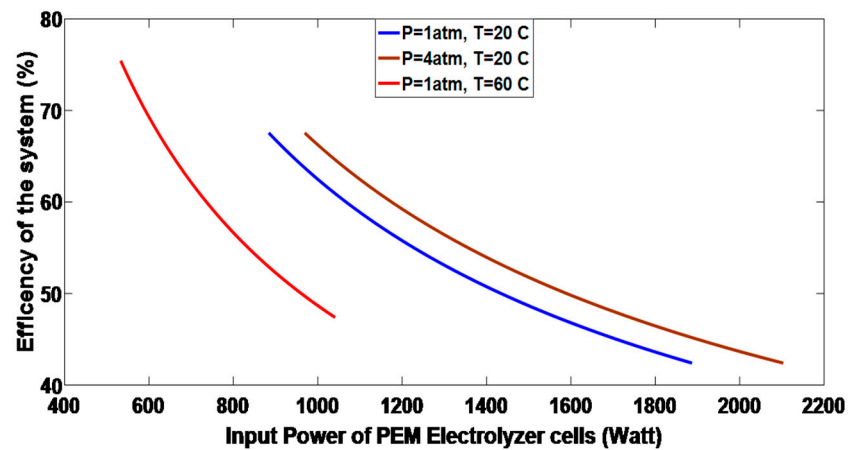
Figure 25. Efficiency of PEM electrolysis vs. the input electrical power of PEM electrolysis at different operating conditions.

Figure 26. Pressure of hydrogen inside the tank at different operating conditions.

The internal resistance of the cell is represented by the slope of the V–I curve in Figure 27. Two different temperatures (20 and 60 degrees Celsius) at the same pressure (1 atm) were tested, as well as two different pressure levels (1 and 4 atm) at the same temperature (20C). The PEM electrolysis cell resistance grew with temperature at the same pressure value, as is shown in the active electrolysis zone, resulting in a lower conductivity. With higher pressures, the cell resistance decreased for the same temperature value, resulting in a higher conductivity.
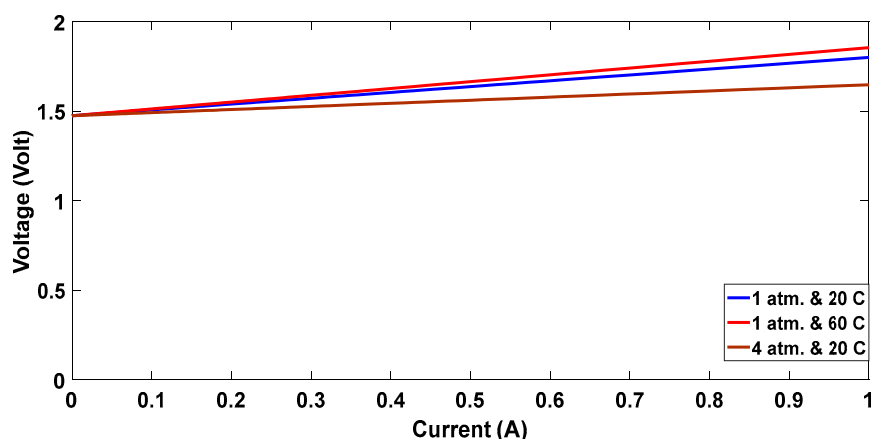
Figure 27. V–I curve of a single PEM electrolysis cell at various operating conditions.

8. Experimental Results

To validate the simulation results and confirm the feasibility of proposed A. Sugeno-type fuzzy inference system (FIS), a laboratory prototype of the IM drive system was built based on the DSPACE DS1104 control board. Using an active-servo motor, different load torque profiles were used to experimentally test the variable speed drive based on the SCIG. Additionally, MATLAB software was used to create the simulation model, and the performance response was compared. Figure 28 shows a photo of the real experimental system. The experimental setup consisted of a three-phase IM (six poles, 1.8 kW, 380 V, and 50 Hz), a three-phase inverter (using a CM50DY-24H MITSUBISHI Module, each 50A/1200V), a servo machine attached to the motor to act as a load (with 0.4 kW, 390 V, a nominal speed of 2000 rpm, a maximum speed of 5000 rpm, and a nominal torque of 10 Nm), a DSPACE DS1104, an incremental encoder (with 5000 rpm, 1024 pulses, and a moment of inertia of 35 gcm^2), and Hall-effect current sensors.

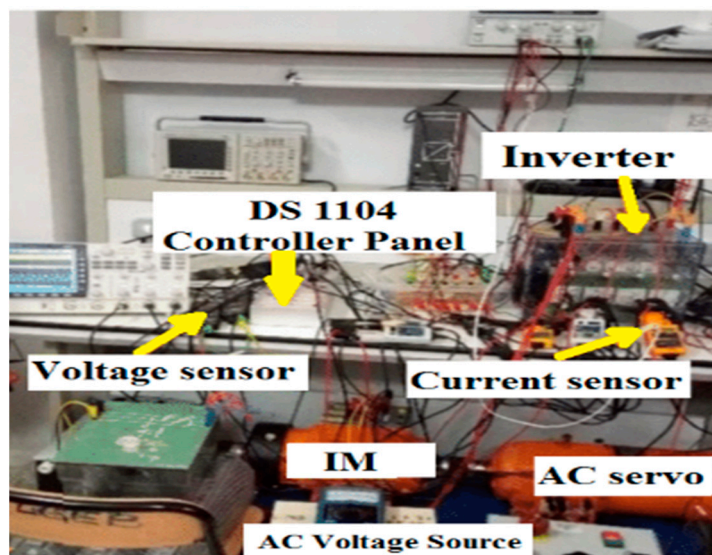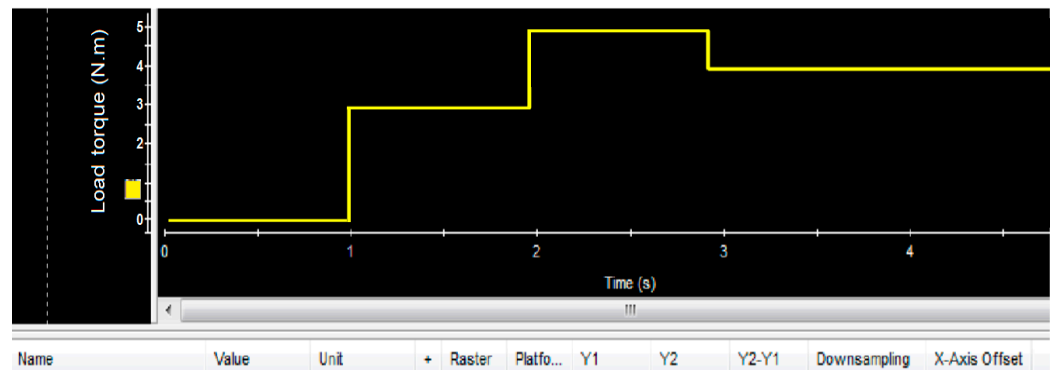**Figure 28.** Photo of the hardware setup of the system.

AciveServo software was used to collect the data. The load profile was assumed to vary for a duration of 5 s, as is shown in Figure 29. There was no load between t = 0 and t = 1 s. At t = 1 s, the load increased suddenly to 3 Nm. At t = 3 s, it reached 5 Nm. Then, until t = 3 s, a constant 5 Nm was maintained. The load then decreased suddenly to 4 Nm.

Figure 29. Hardware co-simulation of the proposed load torque (Nm).

The experimental findings of the motor rotational speed under fuzzy-PID-based PSO and fuzzy-PID-based C-BO are shown in Figure 30 and Table 9. When compared to a conventional fuzzy-PID-based PSO, fuzzy-PID-based C-BO had a lower peak overshoot, less transient ripple, shorter rising and settling times, and was less affected by load variation. The overshoot peak value of speed using fuzzy-PID-based PSO was 9.5 rad/s, while it was 1.2 rad/s for fuzzy-PID-based C-BO. Regarding C-BO, Table 8 shows that the rising time is improved by 5.2% and the peak overshoot is reduced by 87.37%.


(**a**)

(**b**)
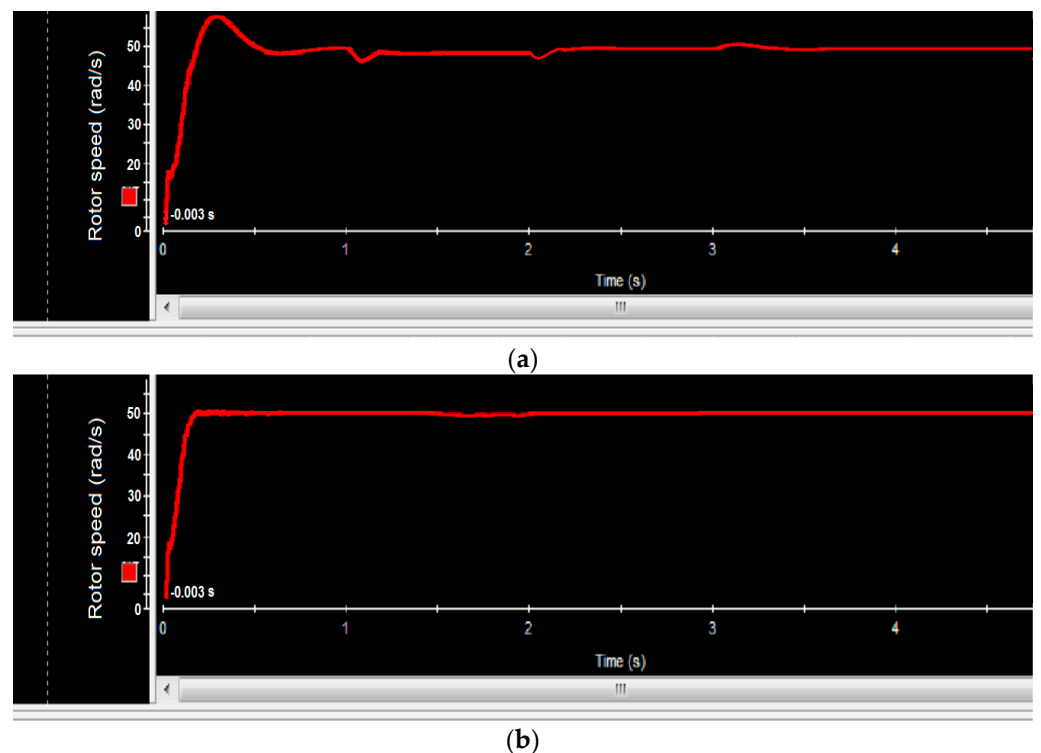
Figure 30. Experimental motor speed under (**a**) fuzzy PID based PSO and (**b**) C-BO-based fuzzy PID.

Table 9. Speed-controller performance at proposed loading.

Type	Tr (ms)	Tp (ms)	Mp (%)	Steady State Error (%)
Fuzzy-PID-based PSO	95.64	213.1	9.5	±0.07
Fuzzy-PID-based C-BO	90.23	95.64	1.2	±0.05

Figure 31 shows the experimental findings of the mechanically developed torque under fuzzy-PID-based PSO and fuzzy-PID-based C-BO. The fuzzy-PID-based C-BO had the disadvantage of having a larger transient ripple when the motor started from zero speed, but it performed better under steady state and load changes. By using fuzzy-PID-based C-BO, the mechanical-torque tracking was improved by 65.32% when compared to the use of fuzzy-PID-based PSO for the small induction motor.
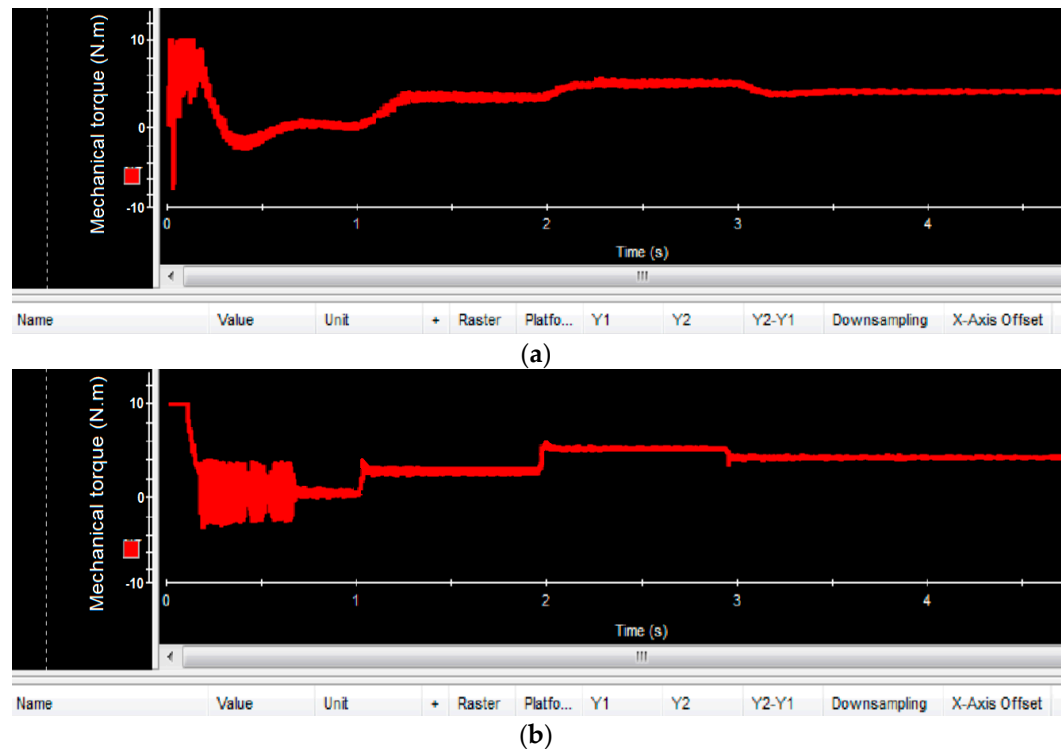
Figure 31. Experimental motor-developed torque under (**a**) fuzzy PID based PSO and (**b**) C-BO-based fuzzy PID.

Based on the experimental results, the system response was enhanced. Better speed and torque-tracking capability were observed and the oscillation rate was reduced when comparing fuzzy-PID-based C-BO with the use of fuzzy PID based PSO.

9. Conclusions

This study demonstrated the success of constructing a solar drive with a backup H_2 energy source, ensuring the service continuity of the solar-powered induction motor. The proposed model was created by converting the highest power from a PV solar array (using MPPT) to a DC/DC current source converter with a PID controller to manage the input current to the PEM electrolysis to obtain the highest hydrogen flow rate. The hydrogen was stored in a hydrogen tank before later being converted to power using a PEM fuel cell. A PEM model was developed for analyzing the impacts of temperature and pressure. The motor is controlled using a variable speed drive based on a brand-new, inspired optimization algorithm (the chaotic billiards optimization (C-BO) approach) to effectively develop the optimal parameters for the fuzzy PID technique to enhance the dynamic response for the solar–hydrogen drive of the induction motor.

In order to correctly design the fuzzy PID speed regulators for the stability improvement of the speed performance, this article provides a novel C-BO method. The induction motor is connected to various types of mechanical loading. The control methodology for these VSCs is a fuzzy-PID approach that has been suitably adjusted by the C-BO. At a quick convergence speed, the C-BO algorithm adjusts the gains of several fuzzy PIDs used in the system. The integrated square error is used as the objective function in a simulation-

based optimization strategy. The augmentation of transient parameters, such as the settling time (Ts), maximum over/undershoots (Mp), and the steady-state error (Ess) of the speed, is a part of the system's stability improvement. By conducting the analysis both experimentally and theoretically, the validity of the proposed control strategy is thoroughly examined.

The simulated and real-time (using a DSPACEDS1104 control board) implementation of an FOC with a fuzzy-PID-based C-BO for squirrel-cage induction motors are detailed in this work. According to the results, fuzzy-PID-based C-BO has a 6.1% faster speed rising time than the fuzzy-PID-based PSO and a 9.5% faster speed rising time than the PI-based PSO speed controller. Moreover, it has a reduced steady-state error and a low overshoot, which is about half of that of the PI–PSO speed regulator. By using fuzzy-PID-based C-BO, the mechanical torque-tracking has been improved by 65.32% when compared to the fuzzy-PID-based PSO used for a small induction motor.

In future work, we plan to investigate the proposed control model of the solar–hydrogen drive of an induction motor under electric vehicles using the Cairo Monorail loading curve as a reference to protect distribution networks from unexplainable actions. We plan to investigate new optimization algorithms and to compare them to the C-BO and PSO results.

Author Contributions: Methodology, R.H.M. and M.N.A.; Software, M.N.A.; Validation, A.M.I.; Resources, B.E.E.; Data curation, R.H.M.; Writing—original draft, A.M.I. and M.N.A.; Writing—review & editing, R.H.M.; Visualization, B.E.E. and R.H.M.; Project administration, B.E.E. and A.M.I.; Funding acquisition, B.E.E. All authors have read and agreed to the published version of the manuscript.

Nomenclature

I_{ph}	is the photo current
I_s	is the first diode saturation current
I_{s2}	is the second diode saturation current
V_t	is the thermal voltage
N_1	is the first diodes quality factor.
N_2	is the second diodes quality factor
V_{phO}	is the solar cell voltage
I_{pho}	is the load output current
R	the universal gas constant
T_m	the operating temperature in (K)
V_T	the tank volume in (m^3)
$z = \dfrac{PV_M}{RT}$	is the compresability constant
V_M	the Molar volume of hydrogen
F	the Faraday constant (96485 C/mole)
e_{rev}	is the reverse voltage
R_i	is the initial PEM cell resistance
I_i	is the input current of the PEM cell
V_{Fuel}	is the hydrogen fuel volume entering the fuel cell
P_{Fuel}	is the hydrogen fuel pressure inside the tank
$U_{F\_H_2}$	is the hydogen utilization factor of fuell cell.
$U_{F\_O_2}$	is the oxygen utilization factor of fuell cell.
$\delta_{\Psi i}$	is the angle between rotor flux and stator current
δ_{Ψ}	is the angle between rotor and stator flux vectors
D_1 and D_2	are the duty ratios for the double − stage converter
E_n	is the Nernst voltage

Δh^{o}	is the enthalpy change
$X\%$	is the rated percentage of hydrogen in the fuel
$Y\%$	is the rated percentage of oxygen in the oxidant
I_{o}	is the exchange current
A	is the Tafel slope
α	is Exchange coefficient
V_{FC}	is rated voltage of the fuel cell
I_{FC}	is rated current of the fuel cell
h	is Plank constant
K	is Boltzman constant
ΔG	is Gibbs Energy
K_{G}	is Gibbs constant
ΔV_{o}	is the stage output ripple voltage
ΔI_{L}	is the stage inductor ripple current
f_{s}	is the switching frequency of the stage transistor
$B_{n.m}^{0}$	is the variable's initial record for n^{th} ball
Var_{m}^{max} and Var_{m}^{min}	are the top and bottom boundaries for the mth variable
β	represents the pocket's fitness value and indicates a selection pressure zero
f_{k}	indicates the fitness of kth pocket
$B_{n,m}^{new}$ and $B_{n,m}^{old}$	signify new and old value of the mth parameter from the ordinary ball
$P_{k,m}^{n}$	sgnify the mth variable of the kth pocket
$rand_{[-ER,ER]}$	Indicates a uniformly distributed random number in the range$[-ER, ER]$
ER	signify error rate
$iter$ and $iter_{max}$	represent the current and max iterative numbers, respectively
$\overrightarrow{v_{n}'}$	is ordinary ball velocity
$\overrightarrow{B_{n}^{old}B_{n}^{new}}$	is the ball movement vector
$\overrightarrow{B_{n}^{old}B_{n}^{new}}$	is the movement unit vector of nth ball ordinary after collision
$\overrightarrow{v_{n+N}'}$ and $\overrightarrow{v_{n+N}}$	is the nth cue ball velocities after and before the collision
B_{n}^{old}	is location of nth cue ball before billiard stick
a	is acceleration rate, and it equals to one

References

1. Szałek, A.; Pielecha, I.; Cieslik, W. Fuel cell electric vehicle (FCEV) energy flow analysis in real driving conditions (RDC). *Energies* **2021**, *16*, 5018.
2. De Souza, L.L.; Lora, E.E.; Palacio, J.C.; Rocha, M.H.; Renó, M.L.; Venturini, O.J. Comparative environmental life cycle assessment of conventional vehicles with different fuel options, plug-in hybrid and electric vehicles for a sustainable transportation system in Brazil. *J. Clean. Prod.* **2018**, *203*, 444–468.
3. Yang, X.; Pang, J.; Teng, F.; Gong, R.; Springer, C. The environmental co-benefit and economic impact of China's low-carbon pathways: Evidence from linking bottom-up and top-down models. *Renew. Sustain. Energy Rev.* **2021**, *13*, 110438.
4. Curtin, J.; McInerney, C.; Gallachóir, B.Ó.; Hickey, C.; Deane, P.; Deeney, P. Quantifying stranding risk for fossil fuel assets and implications for renewable energy investment: A review of the literature. *Renew. Sustain. Energy Rev.* **2019**, *116*, 109402.
5. Olabi, A.G.; Obaideen, K.; Elsaid, K.; Wilberforce, T.; Sayed, E.T.; Maghrabie, H.M.; Abdelkareem, M.A. Assessment of the pre-combustion carbon capture contribution into sustainable development goals SDGs using novel indicators. *Renew. Sustain. Energy Rev.* **2022**, *153*, 111710.
6. He, X.; Wang, F.; Wallington, T.J.; Shen, W.; Melaina, M.W.; Kim, H.C.; De Kleine, R.; Lin, T.; Zhang, S.; Keoleian, G.A.; Lu, X. Well-to-wheels emissions, costs, and feedstock potentials for light-duty hydrogen fuel cell vehicles in China in 2017 and 2030. *Renew. Sustain. Energy Rev.* **2021**, *137*, 110477.
7. Vargas, J.E.; Seabra, J.E. Fuel-cell technologies for private vehicles in Brazil: Environmental mirage or prospective romance? A comparative life cycle assessment of PEMFC and SOFC light-duty vehicles. *Sci. Total Environ.* **2021**, *798*, 149265.
8. Awasthi, A.; Scott, K.; Basu, S. Dynamic modeling and simulation of a proton exchange membrane electrolyzer for hydrogen production. *Int. J. Hydrog. Energy.* **2011**, *36*, 14779–14786.
9. Castiglia, V.; Ciotta, P.; Di Tommaso, A.O.; Miceli, R.; Nevoloso, C. High performance foc for induction motors with low cost atsam3x8e microcontroller. In Proceedings of the 2018 7th International Conference on Renewable Energy Research and Applications (ICRERA), France, 14–17 October **2018**; pp. 1495–1500.
10. Xu, D.; Wang, B.; Zhang, G.; Wang, G.; Yu, Y. A review of sensorless control methods for AC motor drives. *CES Trans. Electr. Mach. Systems.* **2018**, *2*, 104–115.
11. Hannan, M.A.; Ali, J.A.; Mohamed, A.; Hussain, A. Optimization techniques to enhance the performance of induction motor drives: A review. *Renew. Sustain. Energy Rev.* **2018**, *81*, 1611–1626.
12. Saady, I.; Karim, M.; Bossoufi, B.; Motahhir, S.; Adouairi, M.S.; Majout, B.; Lamnadi, M.; Masud, M.; Al-Amri, J.F. Optimization for a photovoltaic pumping system using indirect field oriented control of induction motor. *Electronics* **2021**, *10*, 3076.

13. Errouha, M.; Derouich, A. Study and comparison results of the field oriented control for photovoltaic water pumping system applied on two cities in Morocco. *Bull. Electr. Eng. Inform.* **2019**, *8*, 1206–1212.

14. Massaq, Z.; Abounada, A.; Chbirik, G.; Ramzi, M.; Brahmi, A. Double Stage Solar PV Array Fed Sensorless Vector Controlled Induction Motor for Irrigational Purpose. In Proceedings of the 2019 7th International Renewable and Sustainable Energy Conference (IRSEC), Agadir, Morocco, 27–30 November 2019, pp. 1–6.

15. Tang, Q.; Ge, X.; Liu, Y.C. Performance analysis of two different SVM-based field-oriented control schemes for eight-switch three-phase inverter-fed induction motor drives. In Proceedings of the 2016 IEEE 8th International Power Electronics and Motion Control Conference (IPEMC-ECCE Asia), Hefei, China, 22–26 May 2016, pp. 3374–3378.

16. Dessouky, S.S.; Elbaset, A.A.; Alaboudy, A.H.; Ibrahim, H.A.; Abdelwahab, S.A. Performance improvement of a PV-powered induction-motor-driven water pumping system. In Proceedings of the 2016 Eighteenth International Middle East Power Systems Conference (MEPCON), Cairo, Egypt, 27–29 December 2016; pp. 373–379.

17. Singh, B.; Sharma, U.; Kumar, S. Standalone photovoltaic water pumping system using induction motor drive with reduced sensors. *IEEE Trans. Ind. Appl.* **2018**, *54*, 3645–3655.

18. Ramulu, C.; Sanjeevikumar, P.; Karampuri, R.; Jain, S.; Ertas, A.H.; Fedak, V. A solar PV water pumping solution using a three-level cascaded inverter connected induction motor drive. *Eng. Sci. Technol. Int. J.* **2016**, *19*, 1731–1741.

19. Rahman, S.; Meraj, M.; Iqbal, A.; Tariq, M.; Maswood, A.I.; Ben-Brahim, L.; Al-ammari, R. Design and implementation of cascaded multilevel qZSI powered single-phase induction motor for isolated grid water pump application. *IEEE Trans. Ind. Appl.* **2019**, *56*, 1907–1917.

20. González, E.L.; Llerena, F.I.; Pérez, M.S.; Iglesias, F.R.; Macho, J.G. Energy evaluation of a solar hydrogen storage facility: Comparison with other electrical energy storage technologies. *Int. J. Hydrogen Energy* **2015**, *40*, 5518–5525.

21. Okundamiya, M.S. Size optimization of a hybrid photovoltaic/fuel cell grid connected power system including hydrogen storage. *Int. J. Hydrogen Energy* **2021**, *46*, 30539–30546.

22. Zeb, K.; Ali, Z.; Saleem, K.; Uddin, W.; Javed, M.A.; Christofides, N. Indirect field-oriented control of induction motor drive based on adaptive fuzzy logic controller. *Electr. Eng.* **2017**, *99*, 803–815.

23. Hasanien, H.M.; Muyeen, S.M. Design optimization of controller parameters used in variable speed wind energy conversion system by genetic algorithms. *IEEE Trans. Sustain. Energy* **2012**, *3*, 200–208.

24. Qais, M.H.; Hasanien, H.M.; Alghuwainem, S. Augmented grey wolf optimizer for grid-connected PMSG-based wind energy conversion systems. *Appl. Soft Comput.* **2018**, *69*, 504–515.

25. Hasanien, H.M. Performance improvement of photovoltaic power systems using an optimal control strategy based on whale optimization algorithm. *Electr. Power Syst. Res.* **2018**, *157*, 168–176.

26. Zambrana-Lopez, P.; Fernández-Quijano, J.; Fernandez-Lozano, J.J.; Garcia-Cerezo, A.; Rubio, P.M. Fuzzy logic tuning of a PI controller to improve the performance of a wind turbine on a semi-submersible platform under different wind scenarios. *IFAC-Pap.* **2020**, *53*, 12364–12371.

27. Ustun, S.V.; Demirtas, M. Optimal tuning of PI coefficients by using fuzzy-genetic for V/f controlled induction motor. *Expert Syst. Appl.* **2008**, *34*, 2714–2720.

28. Sahu, R.K.; Panda, S.; Sekhar, G.C. A novel hybrid PSO-PS optimized fuzzy PI controller for AGC in multi area interconnected power systems. *Int. J. Electr. Power Energy Syst.* **2015**, *64*, 880–893.

29. Abedini, M.; Mahmodi, E.; Mousavi, M.; Chaharmahali, I. A novel Fuzzy PI controller for improving autonomous network by considering uncertainty. *Sustain. Energy Grids Netw.* **2019**, *18*, 100200.

30. Kalaam, R.N.; Muyeen, S.M.; Al-Durra, A.; Hasanien, H.M.; Al-Wahedi, K. Optimisation of controller parameters for grid-tied photovoltaic system at faulty network using artificial neural network-based cuckoo search algorithm. *IET Renew. Power Gener.* **2017**, *11*, 1517–1526.

31. Zhao, J.; Lin, M.; Xu, D.; Hao, L.; Zhang, W. Vector control of a hybrid axial field flux-switching permanent magnet machine based on particle swarm optimization. *IEEE Trans. Magn.* **2015**, *51*, 1–4.

32. Taieb, A.; Ferdjouni, A. A new design of fuzzy logic controller optimized by PSO-SCSO applied to SFO-DTC induction motor drive. *Int. J. Electr. Comput. Eng.* **2020**, *10*, 2088–8708.

33. Costa, B.L.; Bacon, V.D.; da Silva, S.A.; Angélico, B.A. Tuning of a PI-MR controller based on differential evolution metaheuristic applied to the current control loop of a shunt-APF. *IEEE Trans. Ind. Electron.* **2017**, *64*, 4751–4761.

34. Kaveh, A.; Khanzadi, M.; Moghaddam, M.R. Billiards-inspired optimization algorithm; a new meta-heuristic method. *Structures* **2020**, *27*, 1722–1739.

35. Anwar, S.; Khan, F.; Zhang, Y.; Djire, A. Recent development in electrocatalysts for hydrogen production through water electrolysis. *Int. J. Hydrogen Energy* **2021**, *46*, 32284–32317.

36. Kumar, S.S.; Himabindu, V. Hydrogen production by PEM water electrolysis–A review. *Mater. Sci. Energy Technol.* **2019**, *2*, 442–454.

37. Fu, Q.; Mabilat, C.; Zahid, M.; Brisse, A.; Gautier, L. Syngas production via high-temperature steam/CO_2 co-electrolysis: An economic assessment. *Energy Environ. Sci.* **2010**, *3*, 1382–1397.

38. Mergel, J.; Carmo, M.; Fritz, D. Status on technologies for hydrogen production by water electrolysis. *Transit. Renew. Energy Syst.* **2013**, 425–450. doi:10.1002/9783527673872.ch22

39. Maskalick, N.J. High temperature electrolysis cell performance characterization. *Int. J. Hydrogen Energy* **1986**, *11*, 563–570.

40. Erdle, E.; Dönitz, W.; Schamm, R.; Koch, A. Reversibility and polarization behaviour of high temperature solid oxide electrochemical cells. *Int. J. Hydrogen Energy* **1992**, *17*, 817–819.

41. Laguna-Bercero, M.A. Recent advances in high temperature electrolysis using solid oxide fuel cells: A review. *J. Power Sources* **2012**, *203*, 4–16.

42. Brezak, D.; Kovač, A.; Firak, M. MATLAB/Simulink simulation of low-pressure PEM electrolyzer stack. *Int. J. Hydrogen Energy* **2022**. https://doi.org/10.1016/j.ijhydene.2022.03.092.

43. Gutiérrez-Martín, F.; Amodio, L.; Pagano, M. Hydrogen production by water electrolysis and off-grid solar PV. *Int. J. Hydrogen Energy* **2021**, *46*, 29038–29048.

44. Wang, C.; Nehrir, M.H. Power management of a stand-alone wind/photovoltaic/fuel cell energy system. *IEEE Trans. Energy Convers.* **2008**, *23*, 957–967.

45. Jahanbakhshi, M.H.; Etezadinejad, M. Modeling and current balancing of interleaved buck converter using single current sensor. In Proceedings of the 2019 27th Iranian Conference on Electrical Engineering (ICEE), Yazd, Iran, 30 April–2 May 2019; pp. 662–667.

46. Ni, M.; Leung, M.K.; Leung, D.Y. Energy and exergy analysis of hydrogen production by a proton exchange membrane (PEM) electrolyzer plant. *Energy Convers. Manag.* **2008**, *49*, 2748–2756.

47. Karami, N.; Outbib, R.; Moubayed, N. Maximum power point tracking with reactant flow optimization of proton exchange membrane fuel cell. *J. Fuel Cell Sci. Technol.* **2013**, *10*, 14.

48. Kourosh Sedghisigarchi, A.F. Dynamic and transient analysis of power distribution systems with fuel cells-part I: Fuel-cell dynamic mode. *IEEE Trans. Energy Convers.* **2004**, *19*, 423–428.

49. Rahman, M.S.; Paul, S.; Riadh, R.R. Study of 1.26 KW–24 VDC Proton Exchange Membrane Fuel Cell's (PEMFC'S) Parameters Output Behavior: Composition & Temperature. *Electr. Comput. Eng. Int. J.* **2015**, *3*, 43–59.

50. Elnaghi, B.E.; Dessouki, M.E.; Abd-Alwahab, M.N.; Elkholy, E.E. Development and implementation of two-stage boost converter for single-phase inverter without transformer for PV systems. *Int. J. Electr. Comput. Eng.* **2020**, *10*, 2088–8708.

51. Elmahgoud, M.; Bossoifi, B.; Taoussi, M.; Elouanjli, N.; Derouich, A. Rotor field oriented control of doubly fed induction motor. In Proceedings of the 2019 5th International Conference on Optimization and Applications (ICOA), Kenitra, Morocco, 25–26 April 2019; pp. 1–6.

52. Carbone, L.; Cosso, S.; Kumar, K.; Marchesoni, M.; Passalacqua, M.; Vaccaro, L. Induction Motor Field-Oriented Sensorless Control with Filter and Long Cable. *Energies* **2022**, *15*, 1484.

53. Marouane, R.; Malika, Z. Particle swarm optimization for tuning PI controller in FOC chain of induction motors. In Proceedings of the 2018 4th International Conference on Optimization and Applications (ICOA), Mohammedia, Morocco, 26–27 April 2018; pp. 1–5.

54. Talla, J.; Leu, V.Q.; Šmídl, V.; Peroutka, Z. Adaptive speed control of induction motor drive with inaccurate model. *IEEE Trans. Ind. Electron.* **2018**, *65*, 8532–8542.

55. Hannan, M.A.; Ali, J.A.; Lipu, H.; Mohamed, A.; Ker, P.J.; Mahlia, I.; Mansor, M.; Hussain, A.; Muttaqi, K.M.; Dong, Z.Y. Role of optimization algorithms based fuzzy controller in achieving induction motor performance enhancement. *Nat. Commun.* **2020**, *11*, 1.

56. Ferdiansyah, I.; Rusli, M.R.; Praharsena, B.; Toar, H.; Purwanto, E. Speed control of three phase induction motor using indirect field oriented control based on real-time control system. In Proceedings of the 2018 10th International Conference on Information Technology and Electrical Engineering (ICITEE), Bali, Indonesia, 24–26 July 2018; pp. 438–442.

57. Landry, J.F.; Dussault, J.P. AI optimization of a billiard player. *J. Intell. Robot. Syst.* **2007**, *50*, 399–417.

58. Lin, F.; Member, S.; Teng, L.; Yu, M. Radial Basis Function Network Control with Improved Particle Swarm Optimization for Induction Generator System. *IEEE Trans. Power Electron.* **2008**, *23*, 2157–2169.

59. Elgbaily, M.; Anayi, F.; Packianather, M. Genetic and particle swarm optimization algorithms based direct torque control for torque ripple attenuation of induction motor. *Mater. Today Proc.* **2022**, *67*, 577–590.

60. Aspalli, M.S.; Patil, S.J. Study of AI and PI controller using SVPWM technique for induction motor speed control. In Proceedings of the International Conference on Electrical Electronics, Communication, Computer, and Optimization Techniques ICEECCOT, Mysuru, India, 15–16 December 2017; pp. 676–681.

61. Behara, R.K.; Saha, A.K. artificial intelligence control system applied in smart grid integrated doubly fed induction generator-based wind turbine: A review. *Energies* **2022**, *15*, 6488.

62. dos Santos Coelho, L.; Alotto, P. Multiobjective electromagnetic optimization based on a nondominated sorting genetic approach with a chaotic crossover operator. *IEEE Trans. Magn.* **2008**, *44*, 1078–1081.

63. Ma, Z.S. Chaotic populations in genetic algorithms. *Appl. Soft Comput.* **2012**, *12*, 2409–2424.